



# Increased efficiency of charge-mediated fusion in polymer/lipid hybrid membranes

Nika Marušič<sup>a</sup>, Lado Otrin<sup>a</sup>, Jonas Rauchhaus<sup>a</sup>, Ziliang Zhao<sup>b,c,d</sup>, Fotis L. Kyriasis<sup>e</sup>, Farzad Hamdi (فرزاد حمدي)<sup>f</sup>, Panagiotis L. Kastiris<sup>e</sup>, Rumiana Dimova<sup>b</sup>, Ivan Ivanov<sup>a,1</sup>, and Kai Sundmacher<sup>a</sup>

Edited by Virgil Percec, University of Pennsylvania, Philadelphia, PA; received December 17, 2021; accepted April 11, 2022 by Editorial Board Member William F. DeGrado

Due to their augmented properties, biomimetic polymer/lipid hybrid compartments are a promising substitute for natural liposomes in multiple applications, but the protein-free fusion of those semisynthetic membranes is unexplored to date. Here, we study the charge-mediated fusion of hybrid vesicles composed of poly(dimethylsiloxane)-graft-poly(ethylene oxide) and different lipids and analyze the process by size distribution and the mixing of membrane species at  $\mu\text{m}$  and nano scales. Remarkably, the membrane mixing of oppositely charged hybrids surpasses by far the degree in liposomes, which we correlate with properties like membrane disorder, rigidity, and ability of amphiphiles for flip-flop. Furthermore, we employ the integration of two respiratory proteins as a functional content mixing assay for different membrane compositions. This reveals that fusion is also attainable with neutral and cationic hybrids and that the charge is not the sole determinant of the final adenosine triphosphate synthesis rate, substantiating the importance of reconstitution environment. Finally, we employ this fusion strategy for the delivery of membrane proteins to giant unilamellar vesicles as a way to automate the assembly of synthetic cells.

polymer | phospholipid | fusion | membrane mixing | ATP

In eukaryotic cells, membrane fusion by SNARE proteins (1) plays a crucial role in various cellular functions, such as exo- and endocytosis, membrane remodeling, cell division, signal transduction, and intracellular trafficking. In addition to fusogenic proteins,  $\text{Ca}^{2+}$  is another important mediator that usually participates in fusion events together with SNAREs; e.g.,  $\text{Ca}^{2+}$  triggers neurotransmitter release during the exocytosis of synaptic vesicles (2). Accompanying players in many charge-related mechanisms are also anionic phospholipids like phosphatidylinositol and phosphatidylserine (PS) (3); e.g., the redistribution of PS in the outer leaflet takes place during apoptosis and syncytial fusion (4). In addition to fusion occurring inside the same organism, viruses have developed their own ways to insert genetic material into the host cell (5). All these natural fusion facilitators offer a diverse toolbox that can be utilized in bottom-up synthetic biology to mimic some of the aforementioned functions. The mechanisms behind salt (6–9), charge (10–12), SNARE (13, 14), and viral (15, 16) fusion of phospholipid compartments have been well characterized and employed for the construction of lifelike functional systems. In this way, integral membrane proteins have been co-reconstituted by SNAREs (17) or delivered to liposomes via electrostatic attraction (18, 19), while  $\text{Mg}^{2+}$  has facilitated the automated formation of droplet-stabilized protocells in microfluidics (20).

Liposomes are essentially reductionist models of natural cells and their membranes. Hence, they serve as workhorses to study membrane proteins (MPs) and interfacial phenomena in general but also as a chassis for the construction of artificial organelles and cells. However, without the natural metabolism for membrane replenishment, the limited chemical stability of liposomes poses limitations. This liability arises from the fact that their building blocks are prone to oxidation and hydrolysis, which may cause destabilization of the membrane and, consequently, leakage of cytosolic cargo and deactivation of the inserted MPs (21–23). To circumvent this issue, lipids have been completely or partially substituted with synthetic copolymers (24–27) to form polymerosomes or hybrids, respectively. The latter mixing strategy uses the synergistic effect of both types of amphiphiles (28) and is especially useful when the polymer environment alone does not well suit certain MPs (24). Polymers may thereby not only contribute to enhanced functional and structural durability but also can endow direct protection against oxidative damage when the synthetic amphiphile dominates the composition (21). Furthermore, the reorganization of hybrid membranes upon protein insertion has been shown to reduce the proton permeability in comparison to proteoliposomes (21)

## Significance

The discovery that amphiphilic polymers, similar to phospholipids, can self-assemble to vesicles has inspired numerous applications. For instance, these polymerosomes are employed for drug delivery due to their increased chemical and mechanical stability. These polymers can be also mixed with lipids to form the so-called hybrid membranes, which provide further biocompatibility, while new properties emerge. However, the fusion of these hybrids is to date barely explored. Herein, we determined that hybrid vesicles made of poly(dimethylsiloxane)-graft-poly(ethylene oxide) and oppositely charged lipids undergo rapid fusion, surpassing the efficiency in natural membranes. We provide biophysical insights into the mechanism and demonstrate that anionic lipids are not strictly required when the process is employed for the integration of membrane proteins.

Author contributions: N.M., L.O., R.D., I.I., and K.S. designed research; N.M., L.O., J.R., Z.Z., F.L.K., and F.H. performed research; N.M., L.O., Z.Z., P.L.K., and I.I. analyzed data; and N.M. and I.I. wrote the paper.

The authors declare no competing interest.

This article is a PNAS Direct Submission. V.P. is a guest editor invited by the Editorial Board.

Copyright © 2022 the Author(s). Published by PNAS. This open access article is distributed under Creative Commons Attribution-NonCommercial-NoDerivatives License 4.0 (CC BY-NC-ND).

<sup>1</sup>To whom correspondence may be addressed. Email: ivanov@mpi-magdeburg.mpg.de.

This article contains supporting information online at <http://www.pnas.org/lookup/suppl/doi:10.1073/pnas.2122468119/-/DCSupplemental>.

Published May 12, 2022.

and has been used for controlled formation of raft-like domains (29). Not only polymers but also dendrimers have been used for the generation of hybrids due to matching thickness, chemical programmability, and excellent stability of the resulting membranes. Thus, their coassembly with bacterial (30) or human cell membranes (31) has offered platforms for MP reconstitution, glycosylation, and cell adhesion. Finally, note that the concept of amphiphile augmentation is not limited to vesicles and has been used in other model systems for MP reconstitution such as nanodiscs (32). When discussing the advantages that polymers bring, the latter are often juxtaposed with lipids with respect to the different thickness and permeability, leading to better mechanical stability. However, the versatility of synthetic amphiphiles allows for the modulation of the mechanical properties by the respective architectures, chemistries, and molar ratios—i.e., polymer membranes are not rigid by default but tunable. This is evident, for instance, in the case of phase separation (33, 34), which is governed by the hydrophobic mismatch between lipids and polymers, and the resulting line tension (35). Thus, changing only the copolymer architecture from triblock to grafted while keeping the building blocks and membrane thickness the same may suffice for more efficient mixing and formation of fewer domains (36).

As discussed above, fusion is one of the most widespread mechanisms for cellular trafficking and therefore represents the most intuitive tool for the integration of functional parts in artificial cells, regardless of the membrane chemistry. In this respect, we recently succeeded in employing SNARE machinery for the fusion of hybrid vesicles made of phosphatidylcholine and poly(dimethylsiloxane)-graft-poly(ethylene oxide) (PDMS-*g*-PEO) (37). Meanwhile, we were unable to fuse these hybrids in the absence of fusogenic proteins; the agitation in salt solutions that induced the successful fusion of pure polymersomes caused only fission when lipids were present (38). To the best of our knowledge, no other attempts for protein-free fusion of mixed polymer/lipid vesicles have been made to date. Therefore, herein we study the fusion of PDMS-*g*-PEO-based hybrids mediated by oppositely charged lipids. We characterize the process by following the evolution of the size distribution, next to membrane and content mixing, whereby the latter is assessed by the functional integration of two respiratory enzymes. Furthermore, we employ this electrostatic cue to overcome the fusion barrier in compartments with low curvature. To this end, we monitor the membrane mixing between micro- and nanocompartments via fluorescence microscopy, whereas cryoelectron microscopy (cryoEM), surface charge, flip-flop, and membrane disorder measurements provide further insights into the role of the synthetic amphiphile. Finally, we apply the charge-mediated fusion of hybrids as a controlled delivery mechanism in a microfluidic setup.

## Results and Discussion

**Small Amounts of Charged Lipids Induce Rapid and Efficient Membrane Mixing in Hybrid Membranes.** The hybrid vesicles used in this study were composed of PDMS<sub>26</sub>-*g*-(PEO<sub>12</sub>)<sub>2</sub> (in the following referred to just as PDMS-*g*-PEO) and 5 to 40 mol% of anionic soy PS or cationic 1,2-dioleoyl-3-trimethylammoniumpropane (DOTAP). For control experiments, zwitterionic (i.e., neutral) 1,2-dioleoyl-*sn*-glycero-3-phosphocholine (DOPC) was used instead of the charged lipids or the polymer. The size evolution and membrane mixing were monitored in ~100 nm large unilamellar vesicles (LUVs), prepared by freeze-thaw and subsequent extrusion, as described in *Materials and Methods*. The size

distribution was assessed by dynamic light scattering (DLS), while the membrane mixing assay was based on the fluorescence resonance energy transfer (FRET) between the donor 7-nitro-2-1,3-benzoxadiazol-4-yl (NBD) and the acceptor lissamine rhodamine B sulfonyl (Rho). Anionic vesicles thus contained both dyes, whereas cationic ones remained dye-free, and total NBD dequenching was obtained by solubilization with Triton X-100 (TTX). To confirm that both lipid dyes are homogeneously distributed in the anionic hybrid membrane, optically accessible giant unilamellar vesicles (GUVs) were prepared by electroformation and analyzed by fluorescence microscopy (*SI Appendix*, Fig. S1).

Targeting primarily a single round of fusion, we first mixed oppositely charged LUVs (tagged with 1.5 mol% of each dye) in molar ratio 1:1 and observed rapid dynamics in all tested amphiphile compositions. In the benchmark liposomes, increasing the amount of charged lipids from 5 to 40 mol% led to higher membrane mixing efficiency, as expected from the higher driving force. However, this was surprisingly not the case for hybrids, in which the highest score ( $49 \pm 1\%$ ) was obtained with 10 mol% of PS/DOTAP and decreased upon further charging (Fig. 1A). We ascribed this effect to trapping and screening of phosphatidylethanolamine-Rho (PE-Rho) and PE-NBD by the charged lipids, which skewed the FRET readout. Therefore, we used higher membrane dilution to facilitate the diffusion of the tagged lipids. Indeed, increasing the amount of nontagged LUVs led to more dequenching (Fig. 1C). Since PDMS-*g*-PEO membranes are slightly negative (21) and PE-Rho and PE-NBD further increase their negativity (37, 38), we tested whether the intrinsic charge of the polymer would suffice for membrane mixing. This hypothesis was confirmed upon mixing the tagged polymersomes with nontagged hybrids containing 5 to 40 mol% cationic lipids, whereby the highest degree (about 20%) of membrane mixing was again at 10 mol% DOTAP loading (*SI Appendix*, Fig. S2).

However, membrane mixing did not always correspond to complete vesicle fusion, as evidenced by the absence of DLS changes in hybrids containing 5 to 10 mol% of charged lipids (Fig. 2; volume distribution in *SI Appendix*, Fig. S3). The size increased only when electrostatic attraction was promoted by higher (20 to 40 mol%) amounts of PS/DOTAP, resulting roughly in a doubling of the vesicle areas. For example, the mean diameter of hybrids containing 30 mol% of charged lipids increased to 173 nm upon fusion, which roughly corresponded to the expected value of 185 nm, calculated by adding the mean vesicle areas. Slightly lower experimental diameters in comparison to the theoretical ones (based on the area constraint) have also been previously observed after SNARE-mediated liposome fusion (39). In parallel, using the volume constraint to calculate the theoretical diameters upon fusion leads to closer agreement with DLS data. However, an additional low-intensity peak at ~5  $\mu\text{m}$  (pronounced in the volume distribution; *SI Appendix*, Fig. S3) suggested that hybrids with the latter compositions did not undergo only binary fusion; therefore, neither type of theoretical values may be used for precise quantification.

To minimize the trapping effect, we reduced the lipid dye concentration to 0.5 mol% in another set of FRET experiments. The dilution indeed improved the assay sensitivity in both hybrids and liposomes, resulting in nearly double the degree of membrane mixing in all tested systems (Fig. 1B). However, the trends in liposomes and hybrids remained the same, and 10 mol% loading of charged lipids in the latter membranes resulted in the highest response ( $79 \pm 3\%$ ) upon

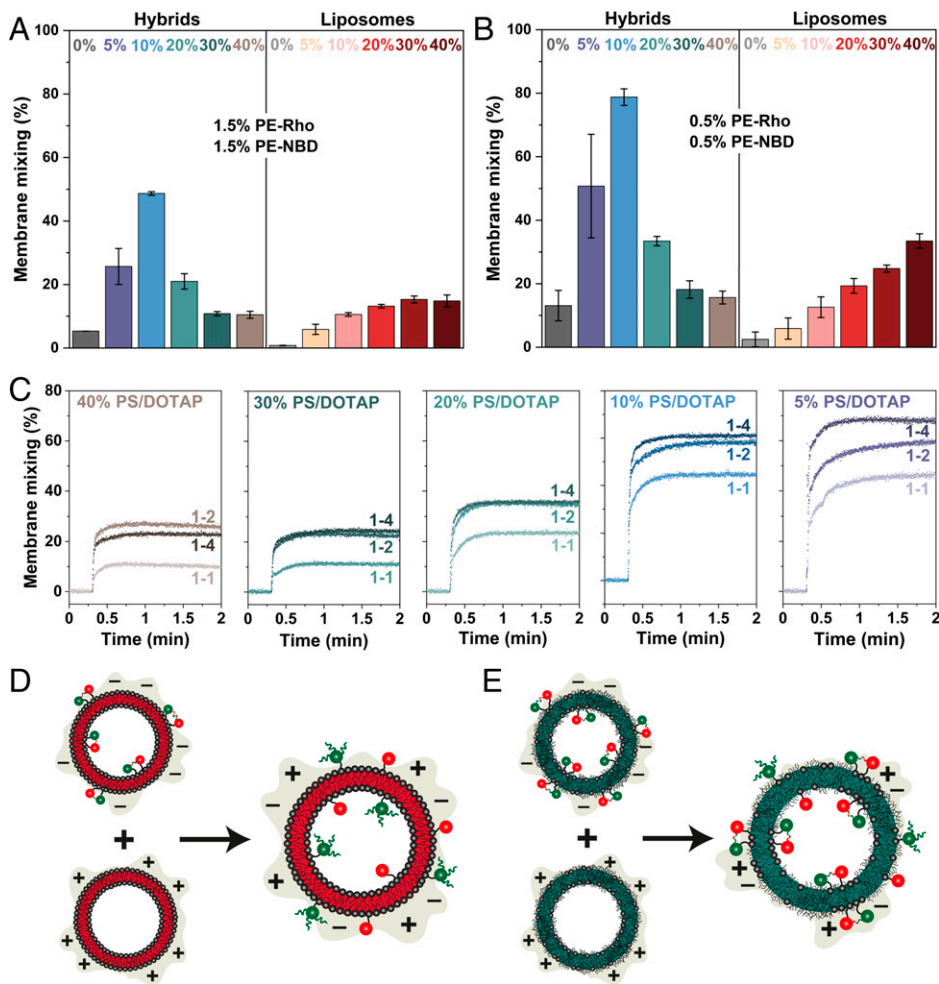


**Fig. 1.** Charge-mediated membrane mixing of hybrid and lipid LUVs with different amounts of charged lipids as assessed from FRET measurements. Hybrid LUVs were composed of 60 to 100 mol% PDMS-*g*-PEO and 0 to 40 mol% DOTAP/soy PS, while lipid LUVs contained 60 to 100 mol% DOPC and 0 to 40 mol% DOTAP/soy PS. (A and B) Membrane mixing degree (after 3 min) of hybrid and lipid LUVs, containing different amounts of charged lipids (0 to 40 mol%), as indicated in the upper part of the graphs, mixed in molar ratio 1:1; the final concentration of LUVs was 100  $\mu$ M. Soy PS-LUVs were tagged with PE-Rho and PE-NBD at two different concentrations. The corresponding time courses are shown in *SI Appendix, Figs. S4 and S5*. (C) Membrane mixing kinetics of differently charged hybrid LUVs at three different molar ratios (1:1, 1:2, 1:4) between the tagged (at fixed NBD concentration) and nontagged populations; the final concentrations of LUVs were 100, 150, or 250  $\mu$ M, respectively. Soy PS-containing LUVs were tagged with 1.5 mol% PE-Rho and PE-NBD. (D) Mechanism of the FRET assay in liposomes. Upon fusion, the lipid dyes are homogeneously distributed in the membrane and NBD is dequenched. (E) Proposed mechanism for the unusual behavior in hybrid LUVs. The lipid dyes are trapped in lipid nanodomains, leading to incomplete NBD dequenching upon vesicle fusion.

equimolar mixing. Furthermore, the latter compositions required a higher amount of surfactant to obtain the maximal NBD fluorescence, even beyond the solubilization point.

We also probed the effect of the surfactant (at 0.5 mol% dye loading) by replacing TTX with octyl glucoside (OG), which led to slower solubilization and required higher concentrations (34–42  $\mu$ L of 10% OG vs. 2 to 4  $\mu$ L of 10% TTX). This was likely due to the lower partitioning coefficient of OG in the membrane (58–75  $M^{-1}$  vs. 6200  $M^{-1}$  for TTX in egg phosphocholine [PC] vesicles) (40). Apart from that, the different detergent did not influence the FRET dependence on the charged lipid loading and only slightly increased the readout magnitude (*SI Appendix, Fig. S6*).

Due to the partial discrepancy between the FRET and DLS results, we further explored the effect of the charge sign on the membrane mixing efficiency. Despite the fact that 10 mol% charged lipids might not suffice for full fusion (Fig. 2), we used this ratio because it provided the highest sensitivity in FRET. For liposomes, it was previously shown that fusion required oppositely charged membranes, whereas the combination of neutral and negative LUVs did not promote membrane or content mixing due to the absence of sufficient electrostatic attraction (18). Here, we confirmed this finding only in part by testing three different charge combinations; the membrane mixing between neutral and cationic liposomes (Fig. 3B) was much slower (and fairly linear) but still reached approximately 10% after prolonged observation (*SI Appendix, Fig. S8*); this is understandable considering that PC membranes are only quasi-neutral as they exhibit small negative charge (see, e.g., [41]).

However, in the case of hybrids, mixing tagged neutral LUVs with nontagged cationic LUVs resulted in a measurable degree of membrane mixing in the first minute of the experiment (Fig. 3A). On the other side, the small changes in the size distributions of both liposomes and hybrids corresponded to the comparatively low loadings of charged lipids (*SI Appendix, Figs. S9 and S10*).

Although the hybrid membrane appears macroscopically homogeneous when the synthetic polymer predominates (26, 33), heterogeneity is defined with respect to the scale. In this regard, different techniques, including small-angle neutron scattering, indicated the presence of nanodomains in hybrid LUVs composed of PDMS-*g*-PEO and 2-dipalmitoyl-sn-glycero-3-phosphocholine (42). We previously also observed nanoscale phase separation in PDMS-*g*-PEO/soy PC LUVs by cryoEM, where the heterogeneity was manifested by interchanging fuzzy (corresponding to the polymer) and clearly defined bilayer domains (21). To reveal whether nanodomains were present in the hybrids used in this study, we performed cryoEM on PDMS-*g*-PEO/DOTAP and PDMS-*g*-PEO/soy PS/PE-Rho/PE-NBD LUVs containing 5 or 30 mol% of charged lipids. Nanodomains with sizes between 3 and 40 nm were found in all four samples (Fig. 4), but LUVs with a smaller loading of charged lipids exhibited a lower amount of nanodomains; the difference was in particular pronounced in the anionic LUVs containing dyes. Moreover, cryoEM data suggested that SNARE-mediated fusion (i.e., pore formation) of such hybrid LUVs often occurred between the lipid and polymer nanodomains (37). Therefore, we believe that fusion in hybrids was

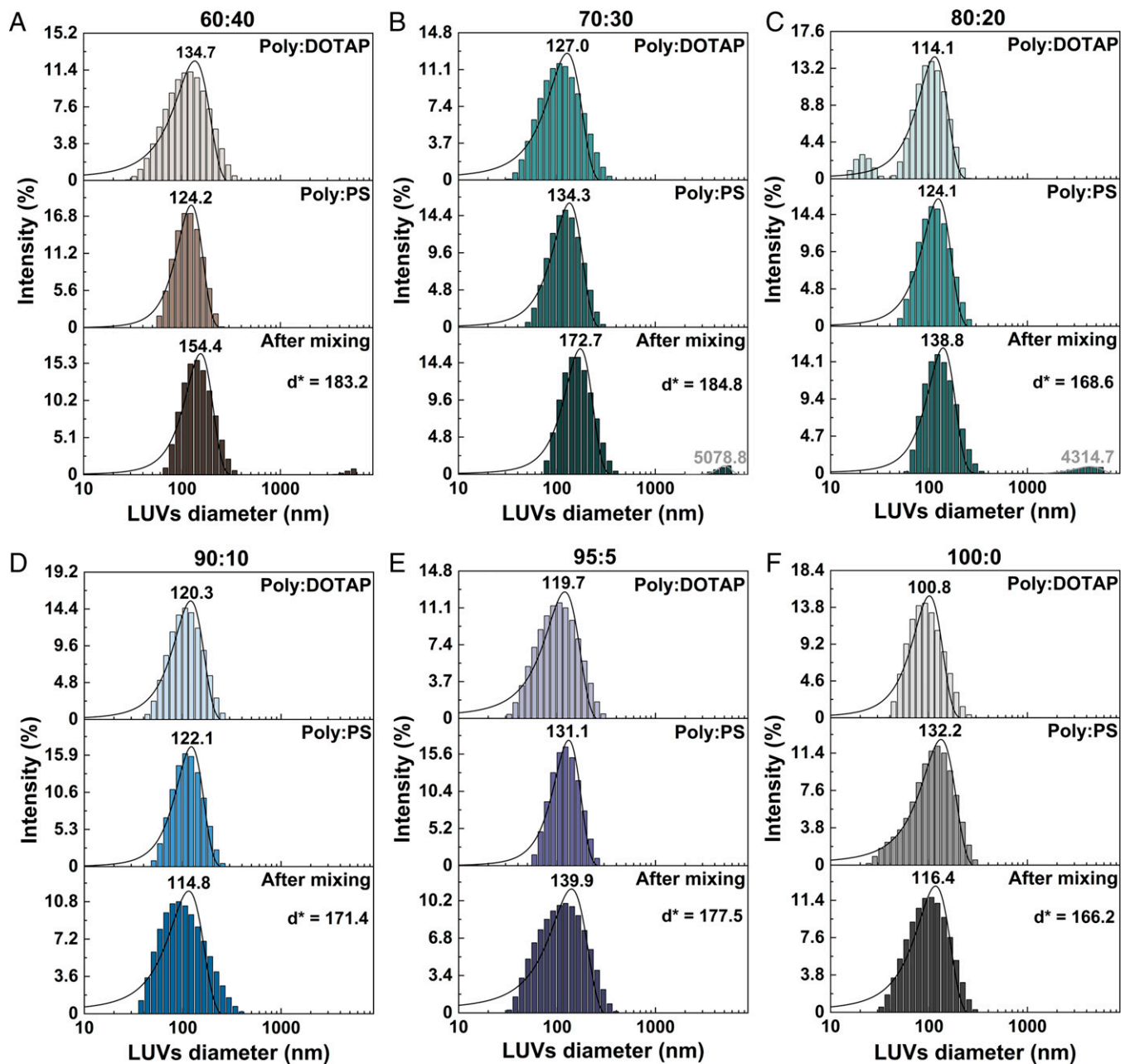


**Fig. 2.** Size changes in differently charged hybrid LUVs upon fusion. The membrane compositions correspond to the ones in Fig. 1A, and Poly denotes PDMS-*g*-PEO. The respective intensity distribution before and after mixing (10 min at 500 rpm) was determined by DLS. The curves show fitted Gaussian distributions, and the mean diameter is indicated above the curves. The mean diameter expected after binary fusion was calculated according to:  $d^* = (d_1^2 + d_2^2)^{1/2}$  and  $d^{**} = (d_1^3 + d_2^3)^{1/3}$  for the area and volume constraints, respectively.

facilitated by the intrinsic negative charge of PDMS-*g*-PEO (compared to DOPC) on the one side, and the formation of lipid nanodomains on the other. However, the latter phase separation also seemed to prevent the full FRET loss because the tagged lipids preferentially partitioned in the charged lipid phase (as sketched in Fig. 1E), whereas the diffusion of PE-Rho and PE-NBD in liposomes was not affected and the dequenching scaled only with the number of (hemi)fusion events (i.e., the degree of membrane mixing). In fact, we observed a similar phenomenon when we reconstituted ubiquinol *bo*<sub>3</sub> oxidase in hybrids, in which the enzyme also sequestered lipids in its vicinity (21).

After fusion, cryoEM of hybrid LUVs containing 5 mol% of charged lipids manifested only early intermediates (referred to as point contact and hemifusion; Fig. 5A), while later fusion intermediates (referred to as pore opening and final configuration;

Fig. 5B) dominated when the charged lipid loading was increased to 30 mol%. This observation is in agreement with the DLS data, and the prospective pore opening snapshots (Fig. 5B) indicated the involvement of lipid nanodomains in the fusion process, similar to our previous observation (37).

**The Synergy between Charge and Mechanical Properties Promotes Fusion of Hybrids.** To elucidate the reasons behind the more efficient membrane mixing in hybrids, we quantified several relevant membrane characteristics. First, we assessed the most apparent cue for charge-mediated fusion by measuring the zeta potentials of LUVs with different membrane compositions in sucrose and in 20 mM Tris-phosphate buffer. The latter was chosen as a model solution with respect to enzyme requirements in the context of cell mimicking.

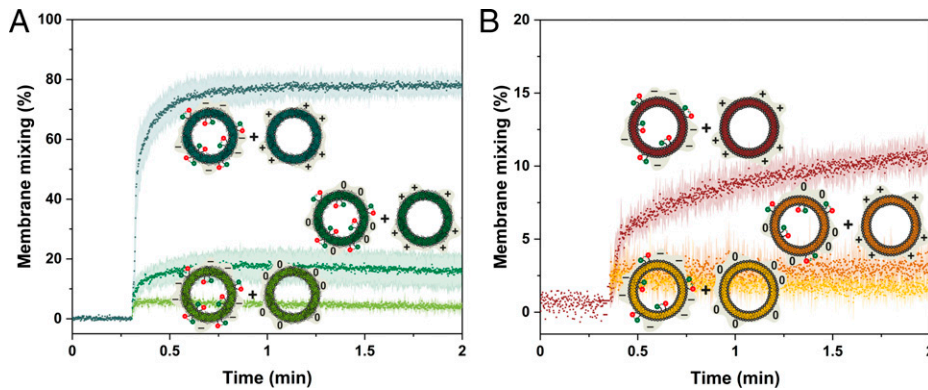


**Fig. 3.** Charge-mediated membrane mixing of anionic (10 mol% soy PS), cationic (10 mol% DOTAP), and neutral (10 mol% DOPC) LUVs. Three combinations were tested: anionic/cationic, neutral/cationic, and anionic/neutral vesicles, and the lipid dyes for FRET were incorporated in either anionic or neutral vesicles at 0.5 mol% loading. LUVs were mixed in molar ratio 1:1, and the final concentration of LUVs was 100  $\mu\text{M}$ . (A) hybrid LUVs and (B) lipid LUVs in 200 mM sucrose. Error bars represent SD from  $n = 3$ .

In sucrose, the effect of the charged lipid loading in hybrids and liposomes was fairly identical, although the negative charge contribution of the polymer was superimposed—it lowered the positive charge of hybrid LUVs overall and increased the negative one in comparison to liposomes (Fig. 6A). The buffer partially neutralized the surface charge of all vesicles as expected; however, its influence was more prominent in the case of hybrids (Fig. 6B). This screening was likely facilitated by better penetration of ions in the expanded hydrophilic layer; this hypothesis is based on the fact that the membrane thickness increased (from  $5.8 \pm 0.3$  nm to  $6.4 \pm 0.3$  nm for cationic hybrid LUVs and from  $5.8 \pm 0.4$  nm to  $6.5 \pm 0.4$  nm for anionic hybrid LUVs; *SI Appendix*, Fig. S11) as revealed by cryoEM data. In parallel, we have shown that salts decreased the bending rigidity (from  $11.6 \kappa_B T$  [21] to  $6.6 \kappa_B T$  [37]) of PDMS-*g*-PEO-containing membranes, which are, in any case, softer than DOPC-containing membranes ( $19.05 \kappa_B T$  [43]). The latter property (i.e., the membrane “softness”) decreases the energy needed for fusion pore opening, as discussed previously (37), and apparently acts in synergy with the effect of the charge in the present case.

Next, we estimated the packing influence of charged and neutral lipids on the hybrid and lipid membranes in 200 mM sucrose by the generalized polarization (GP) value of Laurdan (44). The latter probe is a hydrophobic dye, sensitive to solvent polarity, and its exposure to the aqueous phase in less ordered membranes leads to changes in its fluorescent spectrum. Interestingly, whereas DOTAP had little effect on the membrane order in liposomes likely due to the matching fatty acids, PS progressively packed the latter membranes (Fig. 6D). This outcome is in part counterintuitive because the major component (68%) of the soy PS mixture is diunsaturated and it could be generalized that unsaturation is related to lesser order. For instance, the replacement of one of the acyl chains in DOPC with a saturated one (1-palmitoyl-2-oleoyl-*sn*-glycero-3-phosphocholine [POPC]) caused considerable ordering of the liquid disordered phase in pure membranes (45). However, the negatively charged lipid mixture also contains 10% palmitic chains, and blending of the amphiphiles can potentially amend some irregularities and thus tighten the bilayer. A similar outcome has been demonstrated in the case of PC, whereby natural PC

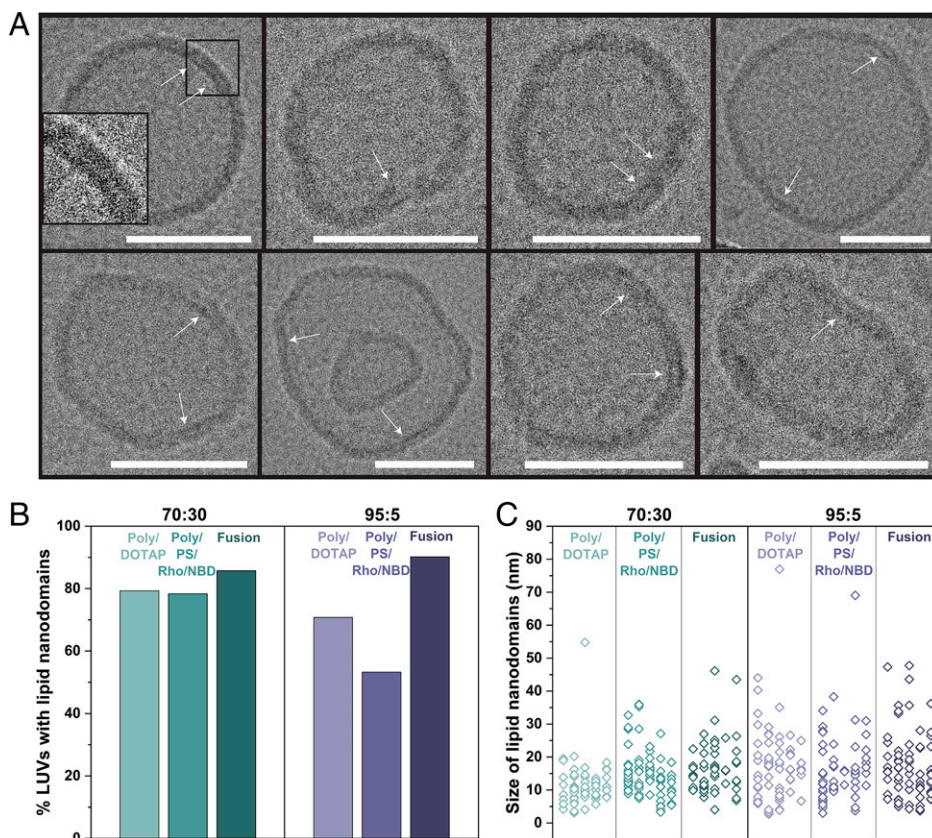


**Fig. 4.** Lipid nanodomains in hybrid LUVs. (A) CryoEM (cryo-Electron Microscopy) images of PDMS-*g*-PEO/DOTAP (70:30, mol%) and PDMS-*g*-PEO/PS/PE-Rho/PE-NBD (69:30:0.5:0.5, mol%) LUVs in 200 mM sucrose. The white arrows show lipid nanodomains, which were designated based on the existence of two distinct contours (see inset). Defocus:  $\sim -2$   $\mu\text{m}$  (Scale bars, 50 nm). (B) Percentage of hybrid LUVs with lipid nanodomains (before and after fusion): PDMS-*g*-PEO/DOTAP (70:30, mol%)  $n = 58$ ; PDMS-*g*-PEO/soy PS/PE-Rho/PE-NBD (69:30:0.5:0.5, mol%)  $n = 60$ ; after fusion (70:30, mol%)  $n = 56$ ; PDMS-*g*-PEO/DOTAP (95:5, mol%)  $n = 65$ ; PDMS-*g*-PEO/soy PS/PE-Rho/PE-NBD (94:5:0.5:0.5, mol%)  $n = 77$ ; after fusion (95:5, mol%)  $n = 61$ . (C) Size of lipid nanodomains in hybrid LUVs with 30 and 5 mol% charged lipids ( $n = 53$  to 83).

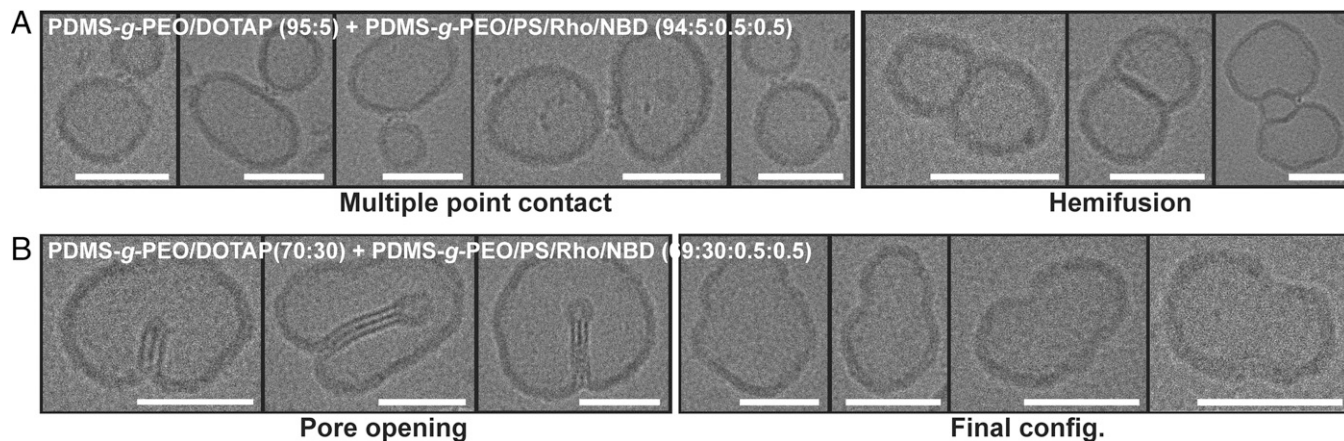


**Fig. 5.** Proposed fusion intermediates. Representative states, imaged by cryoEM, during the fusion of (A) PDMS-*g*-PEO/DOTAP (95:5, mol%) and PDMS-*g*-PEO/soy PS/PE-Rho/PE-NBD (94:5:0.5:0.5, mol%) and (B) PDMS-*g*-PEO/DOTAP (70:30, mol%) and PDMS-*g*-PEO/soy PS/PE-Rho/PE-NBD (69:30:0.5:0.5, mol%) (Scale bars, 50 nm).

mixtures from the liver or brain exhibited higher order than DOPC (46). In parallel, the headgroup in all probability also exercises a packing effect, as shown by the ordering of DOPC/POPC by phosphoethanolamine (PE) (47). On the other side, the impact of charged lipids in hybrids was fairly similar and DOTAP resulted in roughly the same GP as DOPC (Fig. 6D). Furthermore, the individual impact of the main components of the soy PS mixture scaled with the degree of saturation—hybrids containing 18:2 PS exhibited higher disorder than the ones with 18:1 PS, and the palmitic chains further ordered the membranes (*SI Appendix*, Fig. S12). However, the final soy PS mixture did not behave like a weighted average, which suggests that a complex interplay with the polymer dictates the disorder of hybrid membranes. Overall, all types of hybrid mixtures exhibited a higher degree of disorder in comparison to the lipid mixtures, and the packing influence of PS was less pronounced in total. Interestingly, DOPC caused relatively small yet statistically significant ordering of the hybrid membranes, whereas PS did not produce a uniform trend. The latter could be potentially related to enhanced nanoscale phase separation above a certain PS threshold, as discussed in the previous chapter. At 30 mol% charged lipids, the replacement of sucrose with buffer did not exercise a considerable effect (*SI Appendix*, Fig. S13), but the differences can explain the small deviations from previous data on the GP (e.g.,  $-0.29$  in this study vs.  $-0.24$  [45] for DOPC, or  $-0.46$  in this study vs.  $-0.43$  [21] for hybrids containing 30 mol% neutral lipids). Altogether, the overall looser packing of hybrid membranes in comparison to DOPC apparently promotes membrane mixing. Moreover, it can be speculated that the more similar membrane arrangements of anionic and cationic hybrids, manifested by the closer GP values, is another factor that facilitates miscibility in conjunction with electrostatic attraction.

During fusion, the rate and extent of membrane mixing is also determined by the interbilayer (i.e., between the outer layers of separate vesicles) and the transbilayer (i.e., between the outer and inner layers of the same vesicles; also known as flip-flop) transport of the membrane building blocks. Therefore, we studied the kinetics of both processes in liposomes and hybrids by using fatty acid-labeled phospholipids (M-NBD-PE and M-NBD-PC), as previously done for POPC and *Bacillus megaterium* vesicles (48). Due to their shorter acyl chains and consequently increased water solubility, these probes rapidly equilibrate between the outer leaflets of different vesicle populations. The addition of acceptor vesicles (“empty”) to the donor

vesicles (containing PE-Rho and the transport probes) resulted in NBD dequenching profiles that reflected the different behavior of both types of membranes (Fig. 7A). For liposomes, the single exponential profile implied only interbilayer exchange at this timescale. Meanwhile, the biphasic kinetics of hybrids indicated that transbilayer exchange took place at the expected slower rate (Fig. 7A, black trace). The respective rate constants for inter- ( $k_1$ ) and transbilayer ( $k_2$ ) transport are shown in Fig. 7B. Meanwhile, changing the donor/acceptor molar ratio from 0.25 to 0.5 did not have a significant effect on  $k_1$  (*SI Appendix*, Fig. S14). Moreover, no transbilayer transport occurred in hybrids stained with M-NBD-PC (*SI Appendix*, Fig. S15), suggesting that the size of the headgroup played a role in the flip-flop as well. Altogether, cationic vesicles exhibited comparatively faster transport, which correlated to their increased disorder in both natural and hybrid membranes (Fig. 6B). In this regard, the lesser packing of the latter corresponded to shorter half-times [ $t_{1/2} = (\ln 2)/k_1$ ] of interbilayer exchange (0.03 s for M-NBD-PE and 0.02 s for M-NBD-PC) than for liposomes (0.08 to 0.13 s for M-NBD-PE and 0.04 to 0.05 s for M-NBD-PC). The amphiphile transport dictates the membrane mixing primarily during the vesicle docking and hemifusion stages but may influence the full fusion as well. Since there is a disparity between the inner and outer leaflets (e.g., in liposomes with an outer diameter of 100 nm and membrane thickness of 5 nm, the lipids in the outer leaflet are 1.5-fold more than those in the inner leaflet), this imbalance changes upon fusion and has to be compensated by lateral diffusion and flip-flop of membrane building blocks (49). Apparently, the transmembrane mass transport barrier is less pronounced in the case of hybrid membranes in comparison to the intrinsically low rate of leaflet exchange in liposomes, leading to more efficient fusion, in parallel to the relatively fluid character of the membrane, compared to other amphiphilic copolymers (21).

**Fusion of Nano- and Microcompartments—Snapshots at Visible Scale.** As discussed above, vesicle fusion is a ubiquitous natural phenomenon, underpinning processes like communication and trafficking. With regard to the latter aspect, directed fusion can be deliberately employed for the assembly of artificial organelles and artificial cells, for example to deliver membrane proteins into GUVs (18) or to form loaded GUVs via the fusion of small vesicles to droplets (50). Therefore, we next investigated the fusion of hybrid LUVs to hybrid GUVs in different charge combinations. Anionic (PDMS-*g*-PEO/PS) and

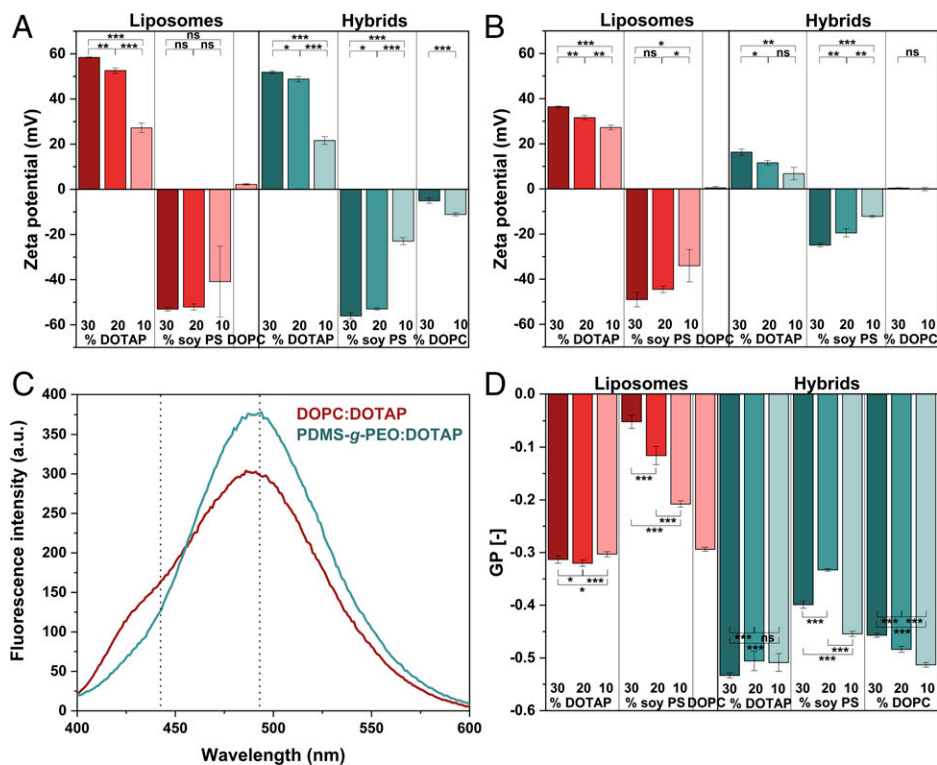


**Fig. 6.** Zeta potential and membrane disorder of lipid (red shades) and hybrid (green shades) LUVs, containing different amounts of cationic (DOTAP), anionic (soy PS), or neutral (DOPC) lipids. Zeta potential was determined in (A) 200 mM sucrose and (B) 20 mM Tris-phosphate buffer (pH 8.0). Bars show the average of two samples, each measured three times, and the average SDs. (C) Fluorescence emission spectra of Laurdan in lipid (DOPC/DOTAP = 70/30 mol%, red shades) and hybrid (PDMS-*g*-PEO/DOTAP = 70/30 mol%, green shades) membranes in 200 mM sucrose. Dotted lines indicate wavelengths used to calculate GP values. (D) GP values of lipid (red shades) and hybrid (green shades) LUVs with different amounts of anionic (PS) or cationic (DOTAP) lipids in 200 mM sucrose. Error bars represent SD from  $n = 3$  to 6. ns, not significant for  $P > 0.05$ ; \* $P \leq 0.05$ ; \*\* $P \leq 0.01$ ; \*\*\* $P \leq 0.001$ .

neutral (PDMS-*g*-PEO/DOPC) GUVs were thereby prepared by electroformation as described in *Materials and Methods*, and their membranes were tagged with PE-NBD; meanwhile, the membranes of cationic (PDMS-*g*-PEO/DOTAP) and neutral LUVs were tagged with PE-Rho. In control experiments, in which LUVs or GUVs were imaged separately, we established that the NBD or Rho signals did not overlap and the two populations were not cross-contaminated (*SI Appendix*, Fig. S16), and anionic GUVs exhibited homogeneous distribution before the fusion experiments (*SI Appendix*, Fig. S17).

After 10 min incubation at 500 rpm of anionic GUVs and cationic LUVs, the red signal of the latter colocalized with the GUV surface, which indicated that full or hemifusion took place (Fig. 8A and *SI Appendix*, Figs. S18 and S19). In particular, we believe that vesicle docking was succeeded by some form of fusion since the latter was previously correlated with the homogeneity of the fluorescence signal (as in the present case) on the one side (12) and the demonstrated readiness of hybrids for membrane mixing (Fig. 1) on the other. In addition, approximately one-quarter of the anionic GUVs were multivesicular upon formation, but after mixing with cationic LUVs, we detected a red signal only on the outer membrane. This finding showed that vesicle engulfment, which was previously observed for cationic LUVs in POPC GUVs (12), did not occur here. In parallel, the incubation of neutral GUVs with cationic LUVs also resulted in colocalization of the two dyes (Fig. 8B and *SI Appendix*, Fig. S20), whereas mixing anionic GUVs with neutral LUVs did not lead to accumulation of the latter on the GUV membrane (Fig. 8C and *SI Appendix*, Fig. S21). The PE-Rho signal intensity varied between the GUVs, likely due to uneven distribution of 1) the LUVs in the sample (only gentle mixing was applied in order to prevent GUV rupture) and 2) the charged lipids between different vesicles. However, quantitative analysis ascertained the trend observed between the different charge combinations (*SI Appendix*, Fig. S22A) and agreed with the membrane mixing results: The highest accumulation of the PE-Rho signal from LUVs was

detected for anionic GUVs and cationic LUVs ( $n = 42$ ), lower for neutral GUVs and cationic LUVs ( $n = 63$ ), and almost negligible for anionic GUVs and neutral LUVs ( $n = 69$ ). This difference was even more pronounced when the background PE-Rho intensity (from nonhemifused/fused LUVs) was taken into account (*SI Appendix*, Fig. S22B).

Next, we investigated the fusion between oppositely charged microcompartments in order to test whether the process would take place with less-curved membranes. GUV-GUV fusion is in fact another promising setup in the context of bottom-up synthetic biology (51) that has been used to, for instance, establish chemical communication between hemifused GUVs (52) or to trigger nanoparticle synthesis in GUVs as microreactors (53). To increase the driving force, we used hybrid GUVs containing 30 mol% charged lipids and induced fusion by mixing a 1:1 vol/vol of both populations and incubating them for 5 min at room temperature, prior to observation. Indeed, oppositely charged hybrid GUVs did fuse, as evidenced by the dye colocalization in the newly formed vesicles (Fig. 9A and *SI Appendix*, Fig. S23). Moreover, replacement of the lipid dye (PE-NBD) with a polymer dye (PDMS-*g*-PEO-fluorescein isothiocyanate [FTIC]) in cationic GUVs further substantiated the macroscopic membrane homogeneity (Fig. 9A and *SI Appendix*, Fig. S24). In this regard, we detected brighter spots in nearly all GUVs containing PE-NBD prior to fusion (*SI Appendix*, Fig. S25), while the distribution of PDMS-*g*-PEO-FTIC remained uniform (*SI Appendix*, Fig. S26). This aggregation may again be ascribed to the formation of lipid domains, which sequestered the lipid dye. Another noteworthy observation was that in some cases, the process was arrested in an intermediate state, evidenced by long contacts between several GUVs, which was ascribed to hemifusion in accordance with the pronounced ability for outer layer mixing in the hybrid membranes (*SI Appendix*, Figs. S24 and S27).

Since certain MPs require specific lipids to retain activity (like cardiolipin for complex I [54]), we also explored the fusion of giant liposomes as optimal protein vehicles with the

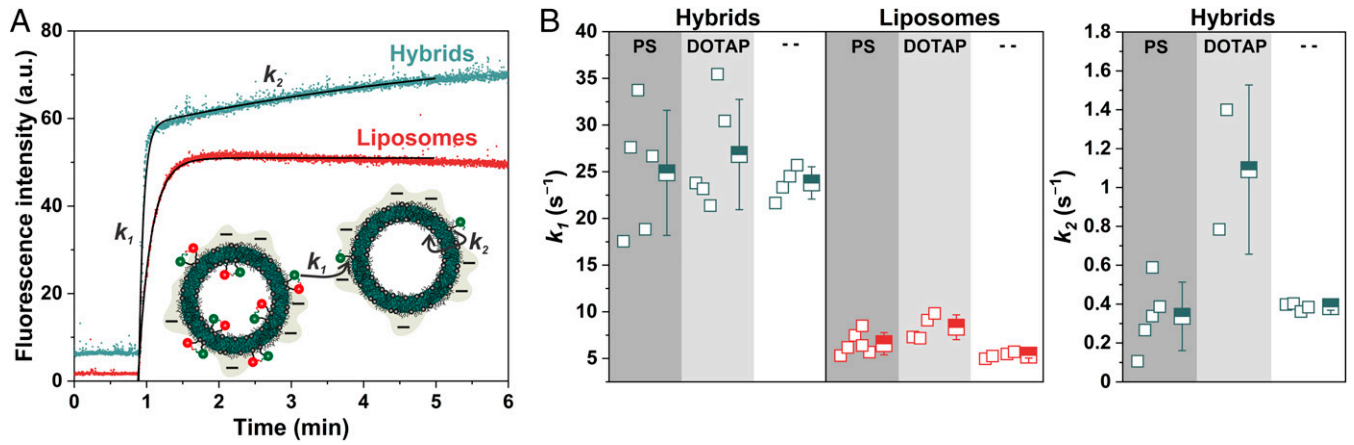


**Fig. 7.** Interbilayer and transbilayer transport of M-NBD-PE. (A) Transport of M-NBD-PE from donor to acceptor anionic LUVs. (B) Rate constants obtained by fitting. LUVs contained 10 mol% soy PS, DOTAP, or DOPC (-); in the case of liposomes, (-) represents 100 mol% DOPC. The values correspond to a donor/acceptor molar ratio of 0.25. Only two of five samples of cationic hybrids could be fitted with a double exponential function, indicating high sample heterogeneity.

hybrid GUVs. To this end, we tested the fusion of positively charged lipid GUVs, tagged with PE-NBD, with negatively charged hybrid GUVs, tagged with PDMS-*g*-PEO-Rho. Upon mixing, we observed a colocalized signal from both dyes, indicating successful fusion. Interestingly, a large portion (~40%) of the fused GUVs contained lipid and polymer domains (Fig. 9B and *SI Appendix*, Fig. S28), which were stable during the time of observation (~3 h). Since we previously demonstrated that membrane proteins may sequester lipids (21), this lipid-hybrid fusion strategy may present a way for phase separation and the concomitant formation of enzyme supercomplexes.

**The Outcome of Content Mixing Assay via Coupled Enzymes Does Not Fully Correlate with the Electrostatic Driving Force.** FRET analysis of LUV populations corroborated more efficient membrane mixing in hybrids compared to liposomes, and optical observation at the GUV scale substantiated that the former membranes did fuse. In order to fully quantify the complete fusion, we applied a functional content mixing assay, which we previously used to probe SNARE-mediated fusion (37). To this end, we employed two membrane proteins with coupled activity—a proton pump (ubiquinol *bo*<sub>3</sub> oxidase) and a proton consumer (*F*<sub>1</sub>*F*<sub>0</sub>-ATP synthase)—which were reconstituted

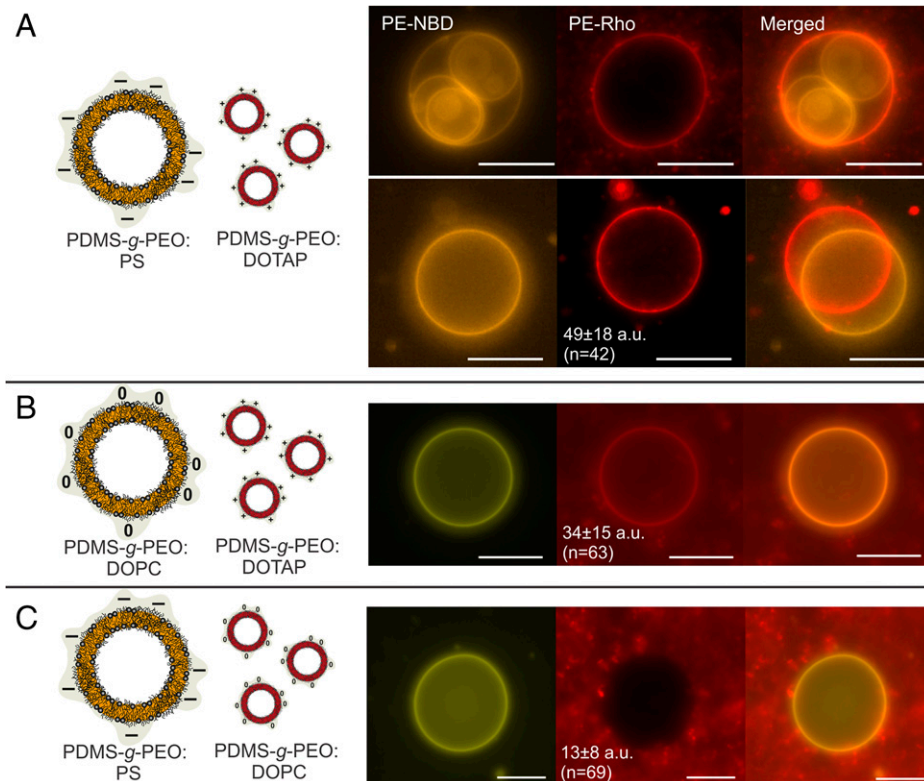


**Fig. 8.** Membrane mixing upon fusion of nano- and microcompartments. Fluorescence microscopy of hybrid GUVs (yellow) mixed with hybrid LUVs (red), both containing 80 mol% PDMS-*g*-PEO. Both GUVs and LUVs were prepared in 200 mM sucrose. Images were taken after incubation at 500 rpm, for 5 min, at room temperature. (A) Anionic hybrid GUVs (20 mol% soy PS) tagged with PE-NBD (0.5 mol%) and cationic hybrid LUV (20 mol% DOTAP) tagged with PE-Rho (0.5 mol%). (B) Neutral hybrid GUVs (20 mol% DOPC) tagged with PE-NBD (0.5 mol%) and cationic hybrid LUV (20 mol% DOTAP) tagged with PE-Rho (0.5 mol%). (C) Anionic hybrid GUVs (20 mol% soy PS) tagged with PE-NBD (0.5 mol%) and cationic neutral LUV (20 mol% DOPC) tagged with PE-Rho (0.5 mol%) (Scale bars, 10  $\mu$ m).

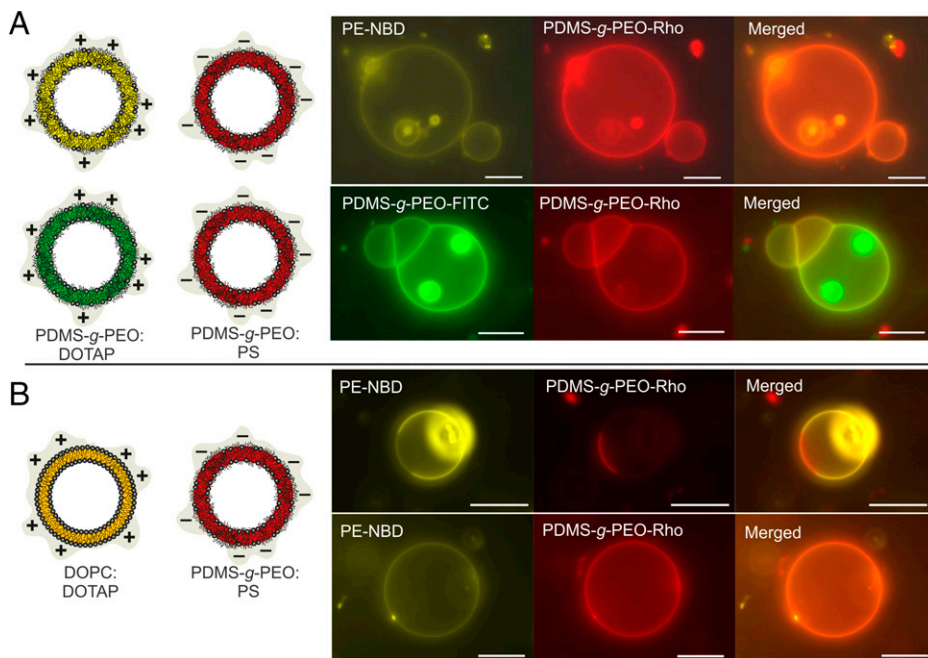


**Fig. 9.** Membrane mixing upon fusion of microcompartments. (A) Cationic hybrid GUVs were labeled either with lipid dye (PE-NBD, yellow) or polymer dye (PDMS-g-PEO-FITC, green). Prior to fusion, no signal in the Rho channel was observed for cationic hybrid GUVs (*SI Appendix*, Fig. S26). Additional micrographs can be seen in *SI Appendix*, Figs. S23 and S24. (B) Two outcomes were observed upon fusion of cationic lipid GUV with anionic hybrid GUVs: Fused GUVs had either homogeneously distributed lipid and polymer or phase separation occurred, and distinct polymer and lipid domains were observed (approximately 40% of evaluated GUVs were heterogeneous). Additional micrographs can be seen in *SI Appendix*, Figs. S28 and S29 (Scale bar, 10  $\mu\text{m}$ ).

into separate compartments and brought together upon fusion. Only if both proteins are present in the membrane and the fused vesicle is proton-tight, then ATPase may use the proton gradient generated by  $bo_3$  oxidase to synthesize ATP. Proton pumping was thereby activated by addition of the electron shuttle ubiquinone 1 ( $Q_1$ ), which was in turn continuously reduced by dithiothreitol, while the ATP synthesis was monitored via luciferin/luciferase assay (Fig. 10A). Since in DLS we did not observe a size increase at lower amounts of charged lipids (Fig. 2), we used hybrid proteo-LUVs containing 30 mol% PS/DOTAP next to DOPC as a neutral control. To accommodate the membrane proteins, the sucrose solution was replaced by Tris-phosphate buffer (20 mM Tris (pH 8.0), 20 mM  $\text{H}_3\text{PO}_4$ ). Since the latter media considerably screened the surface charge, we checked the influence on the membrane mixing efficiency and observed only an approximately 20% decrease compared to sucrose (*SI Appendix*, Fig. S30). In these experiments,  $bo_3$  oxidase was reconstituted in cationic or neutral hybrids and ATPase in anionic or neutral ones (Fig. 10A). This particular setup was chosen because it was previously demonstrated that the ATP synthesis rate was  $\sim 2.5$  times lower when the proton consumer was reconstituted in cationic liposomes (19). In addition, the size of the LUVs before/after reconstitution and upon fusion was analyzed by DLS.

Fusion of oppositely charged hybrids resulted in higher ATP synthesis rates than the case when  $bo_3$  oxidase was present in neutral LUVs, but remarkably, the highest activity was measured when ATPase was reconstituted in neutral LUVs, while the proton pump resided on cationic vesicles (representative measurements shown in Fig. 10B). In these first measurements,  $bo_3$  oxidase was inserted into liposomes by TTX and in hybrids by sodium cholate, while for liposome reconstitution of ATPase we used sodium deoxycholate (SDC), all at their respective saturation points ( $R_{\text{sat}}$ ). In this regard, we checked the influence of the reconstitution protocol for ATPase due to the known fragility of the latter enzyme. This was done by testing four detergents at two different concentrations: at  $R_{\text{sat}}$  and at the solubilization points ( $R_{\text{sol}}$ ), which were determined by titration (*SI Appendix*, Figs. S31–S36). Overall, detergents at  $R_{\text{sat}}$  resulted in higher ATP synthesis rates upon the fusion of oppositely charged proteo-LUVs;

OG performed the best, with the exception of SDC at  $R_{\text{sol}}$  (Fig. 10C). The latter concentration was also associated with larger variability but despite the negative effect on the reproducibility, it was enabled to reach considerably higher activities. Under these conditions, we were able to measure ATP synthesis rates as high as 35  $\text{ATP min}^{-1} \text{ enzyme}^{-1}$  when fusing neutral hybrids with ATPase and cationic hybrids with  $bo_3$  oxidase (Fig. 10D). Meanwhile, mixing cationic proteoliposomes with either neutral or anionic ones produced a similar response.

The behavior in content mixing corresponds to the FRET results shown in the first section with respect to the fact that a positive charge on one of the vesicle populations suffices to induce fusion. This was also confirmed by DLS analysis of hybrid proteo-LUVs, which revealed a size increase only if cationic LUV populations functionalized with a proton pump were employed (Fig. 10E–G and *SI Appendix*, Fig. S37). However, the functional coupling between the enzymes was also affected by the reconstitution of ATPase, which was in turn governed by the lipids and the protocol. It can be generalized that all membrane proteins sequester lipids in their vicinity (the so-called first-shell or annular lipids [55]), and we have demonstrated this also for  $bo_3$  oxidase in hybrid membranes (21). However, the molecular rotor ATPase is known to exhibit even stronger and more specific interactions with certain lipids, which are buried in the c subunit of the  $F_0$  ring (56, 57). Therefore, it can be extrapolated that in the present hybrid system, DOPC provided a more suitable environment for the proton consumer than PS, which lines with the composition of the *Escherichia coli* membrane (i.e., the current source of the protein), dominated by zwitterionic lipids like PE (58). This was further confirmed by the fact that the reconstitution of ATPase in hybrids containing 10 mol% soy PS and 20 mol% DOPC and subsequent fusion with cationic  $bo_3$ -LUVs led to higher ATP synthesis rates than the case when 30 mol% soy PS was used (*SI Appendix*, Fig. S40; DLS can be found in *SI Appendix*, Fig. S41). Furthermore, the multimodal distribution of activity could be related to the nearly complete vesicle dissolution at  $R_{\text{sol}}$ , which would enable two distinct orientations in different combinations. Thus, it appears that the final ATP synthesis rates result from the interplay between the electrostatic driving

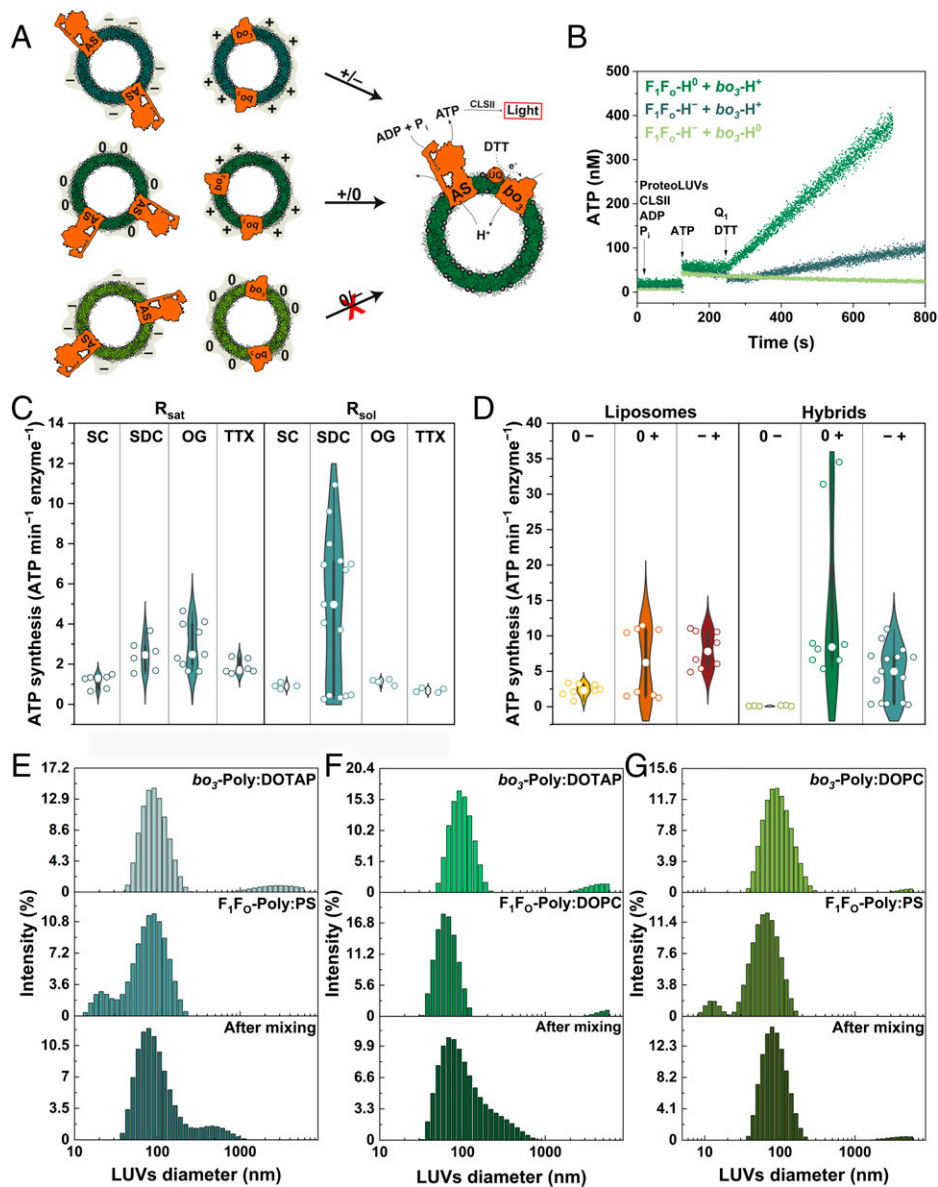


**Fig. 10.** (A) Scheme of the charge-mediated coupling of  $bo_3$  oxidase and  $F_1F_0$ -ATPase. Liposomes were composed of DOPC:DOTAP (70:30), DOPC:PS (70:30) or DOPC, and hybrids of PDMS-*g*-PEO:DOTAP, PDMS-*g*-PEO:PS, or PDMS-*g*-PEO:DOPC (all at 70:30). (B) Representative kinetics of ATP synthesis in hybrids. Liposomes can be seen in *SI Appendix*, Fig. S38. (C) ATP synthesis rates in hybrid LUVs upon variation of the reconstitution conditions for ATPase. The  $bo_3$  oxidase was reconstituted into PDMS-*g*-PEO:DOTAP LUVs by SC at  $R_{sat}$  ( $n = 4$  to 15). (D) ATP synthesis rates in lipid and hybrid LUVs. ATPase was reconstituted by SDC at  $R_{sol}$  ( $n = 6$  to 15). (E-G) Size distributions (DLS) of differently charged hybrid proteo-LUVs before and after fusion. Poly denotes PDMS-*g*-PEO. Liposomes can be seen in *SI Appendix*, Fig. S39.

force and the membrane properties on the one side, and the matching protein environment and orientation on the other.

#### Microfluidic Delivery of Membrane Proteins in Hybrid GUVs.

The charge-mediated fusion of hybrids was not only compatible with membrane proteins but was also used for their functional coupling at the LUV scale. In addition, we demonstrated that LUVs fused to GUVs. Therefore, as a final step, we integrated these two aspects, aiming at the automated assembly of artificial cells and organelles (Fig. 11A). To this end, we employed rectangular microfluidic traps (59) with a gap size of approximately 5  $\mu\text{m}$  between the posts. This setup enabled hydrodynamic control over the LUV delivery, fast exchange of the outer solution, and immobilization of the GUVs. Anionic hybrid GUVs (PDMS-*g*-PEO:PS = 70:30), stained with 0.1 mol% PE-Rho, were prepared via electroformation in 200 mM sucrose and trapped in the microfluidic device. Next, cationic hybrid LUVs (PDMS-*g*-PEO:DOTAP = 70:30), functionalized with ATTO 425-labeled  $bo_3$  oxidase, were flushed into the chip. The latter protein tag was chosen to avoid overlap with the Rho channel. Finally, proteohybrids that did not fuse were washed away with 200 mM sucrose. As a result, the green signal from the protein

accumulated on the outer GUV membrane, which indicated successful delivery to the microcompartment in the timescale of a few minutes (Fig. 11B and *SI Appendix*, Fig. S42). Interestingly, ATTO 425 was detected also in the inner membranes of multivesicular GUVs, which suggested LUV uptake into the outer GUV lumen. In regard to the generally better suitability of natural lipids for protein reconstitution, we also used cationic lipid LUVs (DOPC:DOTAP = 70:30) as delivery vehicles, which resulted in the colocalization of  $bo_3$  oxidase with the GUV membrane as well (Fig. 11C and *SI Appendix*, Fig. S43). These preliminary experiments do not allow one to deduce the prevailing orientation of the proton pump in the GUV membrane or to unequivocally corroborate full fusion, although the latter is implied by the homogeneous distribution of the enzyme on the one side and the DLS and content mixing observations at the LUV scale on the other. In this regard, we believe that the proposed strategy for the automated assembly of membrane machinery can be applied to a variety of proteins, especially with respect to the fact that multiple reconstitution protocols for liposomes exist, whereas the functionality will need additional assessment in every particular case.

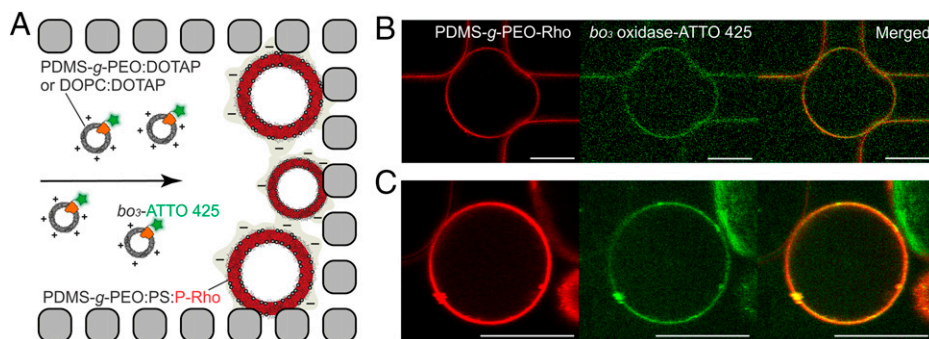


**Fig. 11.** Delivery of  $bo_3$  oxidase into anionic hybrid GUVs trapped in microfluidic device. (A) Schematic representation of the experiment. The  $bo_3$  oxidase was labeled with ATTO 425 (green) and reconstituted into cationic hybrid (B) or lipid (C) LUVs containing 30 mol% DOTAP. Hybrid GUVs were tagged with 0.1 mol% PDMS-*g*-PEO-Rho (P-Rho, red) (Scale bar, 10  $\mu$ m). Micrographs of hybrid GUVs before flushing with proteo-LUVs are shown in *SI Appendix, Figs. S44 and S45*.

## Conclusions

We studied the charge-mediated fusion of PDMS-*g*-PEO-based hybrid LUVs and observed a rapid and significantly higher (6 $\times$ ) degree of membrane mixing in comparison to the benchmark liposomes, which we correlated with membrane properties like increased disorder, lower rigidity, and faster flip-flop. The latter properties arose from the specific architecture and relatively low molecular weight of the graft copolymer, which in turn appeared to result in lower chain entanglement, compared to the commonly used di- and triblocks. Interestingly, the membrane mixing of the present semisynthetic membranes did not scale with the charged lipid loadings (i.e., the electrostatic driving force), which suggested sequestration of the labeled lipids in nanoscopic domains. In the case of fusion of the lipid and hybrid GUVs, this phase separation effect even scaled to optically detectable dimensions, which provides a strategy for the deliberate formation of rafts. While the membrane mixing assay is indicative for the initial stages of fusion, and apposed GUVs (likely arrested in a hemifusion state) were indeed occasionally observed, we also corroborated the complete fusion of the hybrid vesicles by a specific content mixing assay, based on the functional coupling of two respiratory enzymes. Surprisingly, the highest activity was measured upon the fusion of neutral and positively charged hybrids, which we ascribed to the sensitivity of ATP synthase to the lipid nature and the reconstitution conditions. In this regard, the fact that the charge-mediated fusion of hybrids is not limited to oppositely charged membranes opens up more possibilities for fine-tuning of the reconstitution platforms (e.g., when the protein is incompatible with certain membrane composition). Overall, the separate insertion of membrane proteins with distinct membrane requirements and their subsequent integration enables one to overcome the limitations of simultaneous coreconstitution and achieve improved functionality, a notion we also substantiated in the case of hybrid membranes with augmented properties. Moreover, we showed that this integration strategy can be automated by microfluidic means. These results have implications not only for the assembly of artificial organelles and cells; they can also be extrapolated to conventional biotechnological and biomedical applications. In fact, complexes of cationic lipids with DNA are often used for transfection (60–63), which opens the possibility to employ charge-mediated hybrid fusion for gene therapy (64) and interference of extracellular signaling pathways.

## Materials and Methods

**Monitoring of Membrane Mixing of LUVs via FRET.** For preparation of LUVs, see *SI Appendix*. Membrane mixing was monitored via FRET between donor NBD and acceptor Rho by exciting NBD and measuring its emission

(460/535 nm) in 1.5 mL quartz cuvettes at constant stirring at room temperature. The final measurement volume was 800  $\mu$ L. The baseline was recorded with tagged LUVs, diluted at a lipid/polymer concentration of 50  $\mu$ M. Next, non-tagged LUVs were added (at final lipid/polymer concentration 50, 100, or 250  $\mu$ M) and NBD fluorescence dequenching was monitored for 4 to 10 min. To obtain 100% NBD dequenching, Triton X-100 (10%) was added in 5  $\mu$ L steps until reaching maximum NBD fluorescence. Data are presented as the average of three repeats with SD.

**Determination of LUV Size and Zeta Potential Measurements.** The size and dispersity of (proteo)LUVs before and after fusion were determined by DLS. Both DLS and zeta potential measurements were performed using a Zetasizer Nano ZS (Malvern, Worcestershire, UK). Details are available in *SI Appendix*.

**Determination of Membrane Disorder by Laurdan.** The disorder of the membranes was determined with a polarity-sensitive fluorescent probe Laurdan (6-dodecanoyl-2-dimethylaminonaphthalene), as described previously (21). Measurements were done in 200 mM sucrose.

**Analysis of Interbilayer and Transbilayer Transport of M-NBD-Phospholipids.** Transport assay was performed in the fluorescence spectrophotometer Varian Cary Eclipse (Agilent) at an excitation of 460 nm and an emission of 533 nm for M-NBD-PE and at an excitation of 464 nm and an emission of 531 nm for M-NBD-PC (10/20 nm slit width) at constant stirring. Details are available in *SI Appendix*.

**Charge-Mediated Hybrid GUV-LUV and GUV-GUV Fusion.** Details about the preparation of GUVs and LUVs are available in *SI Appendix*. GUV-GUV fusion was analyzed by fluorescent microscopy. Micrographs of hybrid GUVs were recorded on a Zeiss Axio Imager M1 equipped with a digital AxioCam MRm camera (FireWire 1394a). The vesicles were observed with  $\times 100/1.3$  objective lens. Excitation was provided by an HBO 100 short-arc 100 W mercury lamp. Two different filter sets (Zeiss) were used to detect a signal from PDMS-*g*-PEO-Rho/PE-Rho (excitation = 540 nm, emission = 580 nm), PDMS-*g*-PEO-FITC/PE-NBD (excitation = 490 nm, emission = 525 nm), or both.

### Functional Coupling of $bo_3$ Oxidase and $F_1F_0$ -ATPase.

**Preparation and solubilization of LUVs, and proteins reconstitution.** Details about the preparation and solubilization of LUVs used for proteins reconstitution are available in *SI Appendix*. The  $bo_3$  oxidase and  $F_1F_0$ -ATPase were inserted into LUVs via detergent-mediated reconstitution; details are available in *SI Appendix*.

**Charge-mediated fusion of  $bo_3$ -LUVs and  $F_1F_0$ -LUVs.** To fuse charged liposomes or hybrids, 20  $\mu$ L of cationic  $bo_3$ -LUVs was mixed with 20  $\mu$ L anionic  $F_1F_0$ -LUVs and vortexed at 500 rpm for 10 min. For a control, neutral  $bo_3$ -LUVs were mixed with anionic  $F_1F_0$ -LUVs and cationic  $bo_3$ -LUVs were mixed with neutral  $F_1F_0$ -LUVs.

**Respiratory-driven ATP synthesis measurements.** Measurements of respiration-driven ATP production were performed as described previously (26), with slight modification (*SI Appendix*).

**Delivery of  $bo_3$  Oxidase into Hybrid GUVs.** Details about the preparation of  $bo_3$ -ATTO425-LUVs and anionic GUVs are available in *SI Appendix*. Fusion between  $bo_3$ -ATTO425-LUVs and GUVs was monitored as follows. Anionic hybrid GUVs (PDMS-*g*-PEO:soy PS = 70:30, mol%) in 200 mM sucrose were loaded into the chip reservoir and flowed through the channels to occupy the traps. After trapping GUVs,  $bo_3$ -ATTO425-LUVs were flushed into the chip at a flow rate of

0.5  $\mu\text{L min}^{-1}$ , and fusion was monitored via fluorescence of ATTO 425 (excitation = 458, emission = 470 to 510 nm). After ~20 min, nonfused  $bo_3$ -LUVs were flushed away with 200 mM sucrose.

**Data Availability.** All study data are included in the article and/or *SI Appendix*.

**ACKNOWLEDGMENTS.** This work is part of the MaxSynBio consortium, which is jointly funded by the Federal Ministry of Education and Research (BMBF) of Germany and the Max Planck Society. In addition, this research was supported by the EU program European Regional Development Fund of the German Federal State Saxony-Anhalt within the Research Center of Dynamic Systems. K.S. acknowledges the support by the Max Planck School Matter to Life, a joint graduate program of German Universities and Research Organizations. P.L.K., F.H., and F.L.K. acknowledge funding by DFG (project number 391498659, RTG 2467), BMBF (ZIK program, grant number 02222HN23), the European Regional

Development Funds for Saxony-Anhalt (grant number EFRE: ZS/2016/04/78115), and Martin Luther University Halle-Wittenberg. The authors are grateful to Claudia Bednarz for isolation and purification of  $bo_3$  oxidase and  $F_1F_0$ -ATPase and to the group of Dr. Steffen Klamt (Analysis and Redesign of Biological Networks, Max Planck Institute for Dynamics of Complex Technical Systems) for allowing access to their fluorescence microscope and fluorescence spectrophotometer.

Author affiliations: <sup>a</sup>Process Systems Engineering, Max Planck Institute for Dynamics of Complex Technical Systems, 39106 Magdeburg, Germany; <sup>b</sup>Department of Theory and Bio-Systems, Max Planck Institute of Colloids and Interfaces, Science Park Golm, 14476 Potsdam, Germany; <sup>c</sup>Leibniz Institute of Photonic Technology e.V., 07745 Jena, Germany; <sup>d</sup>Faculty of Physics and Astronomy, Institute of Applied Optics and Biophysics, Friedrich Schiller University Jena, 07743 Jena, Germany; and <sup>e</sup>Interdisciplinary Research Center HALOmom and Institute of Biochemistry and Biotechnology, Martin Luther University Halle-Wittenberg, Biozentrum, 06120 Halle/Saale, Germany

1. R. Jahn, R. H. Scheller, SNAREs—Engines for membrane fusion. *Nat. Rev. Mol. Cell Biol.* **7**, 631–643 (2006).
2. R. Jahn, T. Lang, T. C. Südhof, Membrane fusion. *Cell* **112**, 519–533 (2003).
3. M. Leabu, Membrane fusion in cells: Molecular machinery and mechanisms. *J. Cell. Mol. Med.* **10**, 423–427 (2006).
4. B. Huppertz, C. Bartz, M. Kokozidou, Trophoblast fusion: Fusogenic proteins, syncytins and ADAMs, and other prerequisites for syncytial fusion. *Micron* **37**, 509–517 (2006).
5. S. C. Harrison, Viral membrane fusion. *Virology* **479–480**, 498–507 (2015).
6. D. A. Kendall, R. C. MacDonald, A fluorescence assay to monitor vesicle fusion and lysis. *J. Biol. Chem.* **257**, 13892–13895 (1982).
7. J. Wilschut, N. Düzigünes, R. Fraley, D. Papahadjopoulos, Studies on the mechanism of membrane fusion: Kinetics of calcium ion induced fusion of phosphatidylserine vesicles followed by a new assay for mixing of aqueous vesicle contents. *Biochemistry* **19**, 6011–6021 (1980).
8. N. Düzigünes *et al.*, Calcium- and magnesium-induced fusion of mixed phosphatidylserine/phosphatidylcholine vesicles: Effect of ion binding. *J. Membr. Biol.* **59**, 115–125 (1981).
9. D. Papahadjopoulos, G. Poste, B. E. Schaeffer, W. J. Vail, Membrane fusion and molecular segregation in phospholipid vesicles. *Biochim. Biophys. Acta* **352**, 10–28 (1974).
10. D. P. Pantazatos, R. C. MacDonald, Directly observed membrane fusion between oppositely charged phospholipid bilayers. *J. Membr. Biol.* **170**, 27–38 (1999).
11. D. P. Pantazatos, S. P. Pantazatos, R. C. MacDonald, Bilayer mixing, fusion, and lysis following the interaction of populations of cationic and anionic phospholipid bilayer vesicles. *J. Membr. Biol.* **194**, 129–139 (2003).
12. R. B. Lira, T. Robinson, R. Dimova, K. A. Riske, Highly efficient protein-free membrane fusion: A giant vesicle study. *Biophys. J.* **116**, 79–91 (2019).
13. S. Koike, R. Jahn, SNAREs define targeting specificity of trafficking vesicles by combinatorial interaction with tethering factors. *Nat. Commun.* **10**, 1608 (2019).
14. C. Ungerermann, D. Langosch, Functions of SNAREs in intracellular membrane fusion and lipid bilayer mixing. *J. Cell Sci.* **118**, 3819–3828 (2005).
15. D. L. Floyd, J. R. Ragains, J. J. Skehel, S. C. Harrison, A. M. van Oijen, Single-particle kinetics of influenza virus membrane fusion. *Proc. Natl. Acad. Sci. U.S.A.* **105**, 15382–15387 (2008).
16. I. S. Kim *et al.*, Mechanism of membrane fusion induced by vesicular stomatitis virus G protein. *Proc. Natl. Acad. Sci. U.S.A.* **114**, E28–E36 (2017).
17. G. Nordlund, P. Bizezinski, C. von Ballmoos, SNARE-fusion mediated insertion of membrane proteins into native and artificial membranes. *Nat. Commun.* **5**, 4303 (2014).
18. O. Biner, T. Schick, Y. Müller, C. von Ballmoos, Delivery of membrane proteins into small and giant unilamellar vesicles by charge-mediated fusion. *FEBS Lett.* **590**, 2051–2062 (2016).
19. R. R. Ishmukhametov, A. N. Russell, R. M. Berry, A modular platform for one-step assembly of multi-component membrane systems by fusion of charged proteoliposomes. *Nat. Commun.* **7**, 13025 (2016).
20. M. Weiss *et al.*, Sequential bottom-up assembly of mechanically stabilized synthetic cells by microfluidics. *Nat. Mater.* **17**, 89–96 (2018).
21. N. Marušić *et al.*, Constructing artificial respiratory chain in polymer compartments: Insights into the interplay between  $bo_3$  oxidase and the membrane. *Proc. Natl. Acad. Sci. U.S.A.* **117**, 15006–15017 (2020).
22. A. W. Girotti, Mechanisms of lipid peroxidation. *J. Free Radic. Biol. Med.* **1**, 87–95 (1985).
23. E. Schnitzer, I. Pinchuk, D. Lichtenberg, Peroxidation of liposomal lipids. *Eur. Biophys. J.* **36**, 499–515 (2007).
24. S. Khan, M. Li, S. P. Muench, L. J. Jeuken, P. A. Beales, Durable proteo-hybrid vesicles for the extended functional lifetime of membrane proteins in bionanotechnology. *Chem. Commun. (Camb.)* **52**, 11020–11023 (2016).
25. C. Kleineberg *et al.*, Light-driven ATP regeneration in diblock/grafted hybrid vesicles. *ChemBioChem.* **21**, 2149–2160 (2020).
26. L. Otrin *et al.*, Toward artificial mitochondrion: Mimicking oxidative phosphorylation in polymer and hybrid membranes. *Nano Lett.* **17**, 6816–6821 (2017).
27. A. Graff *et al.*, Amphiphilic copolymer membranes promote NADH:ubiquinone oxidoreductase activity: Towards an electron-transfer nanodevice. *Macromol. Chem. Phys.* **211**, 229–238 (2010).
28. J.-F. Le Meins, C. Schatz, S. Lecommandoux, O. Sandre, Hybrid polymer/lipid vesicles: State of the art and future perspectives. *Mater. Today* **16**, 397–402 (2013).
29. J. Kowal, D. Wu, V. Mikhalevich, C. G. Palivan, W. Meier, Hybrid polymer-lipid films as platforms for directed membrane protein insertion. *Langmuir* **31**, 4868–4877 (2015).
30. Q. Xiao *et al.*, Bioactive cell-like hybrids coassembled from (glyco)dendrimerosomes with bacterial membranes. *Proc. Natl. Acad. Sci. U.S.A.* **113**, E1134–E1141 (2016).
31. S. S. Yadavalli *et al.*, Bioactive cell-like hybrids from dendrimerosomes with a human cell membrane and its components. *Proc. Natl. Acad. Sci. U.S.A.* **116**, 744–752 (2019).
32. A. Chen, E. J. Majdinasab, M. C. Fiori, H. Liang, G. A. Altenberg, Polymer-encased nanodiscs and polymer nanodiscs: New platforms for membrane protein research and applications. *Front. Bioeng. Biotechnol.* **8**, 598450 (2020).
33. M. Chemin, P.-M. Brun, S. Lecommandoux, O. Sandre, J.-F. Le Meins, Hybrid polymer/lipid vesicles: Fine control of the lipid and polymer distribution in the binary membrane. *Soft Matter* **8**, 2867–2874 (2012).
34. J. Nam, P. A. Beales, T. K. Vanderlick, Giant phospholipid/block copolymer hybrid vesicles: Mixing behavior and domain formation. *Langmuir* **27**, 1–6 (2011).
35. M. Fauquignon, E. Ibarboure, J.-F. Le Meins, Hybrid polymer/lipid vesicles: Influence of polymer architecture and molar mass on line tension. *Biophys. J.* **121**, 61–67 (2022).
36. T. P. Dao *et al.*, Mixing block copolymers with phospholipids at the nanoscale: From hybrid polymer/lipid wormlike micelles to vesicles presenting lipid nanodomains. *Langmuir* **33**, 1705–1715 (2017).
37. L. Otrin *et al.*, En route to dynamic life processes by SNARE-mediated fusion of polymer and hybrid membranes. *Nat. Commun.* **12**, 4972 (2021).
38. N. Marušić *et al.*, Fusion-induced growth of biomimetic polymersomes: Behavior of poly(dimethylsiloxane)-poly(ethylene oxide) vesicles in saline solutions under high agitation. *Macromol. Rapid Commun.* **43**, e2100712 (2022).
39. B. Kong, Y. Yang, D. H. Kweon, Dynamic light scattering analysis to dissect intermediates of SNARE-mediated membrane fusion. *Methods Mol. Biol.* **1860**, 53–69 (2019).
40. J. Lasch, Interaction of detergents with lipid vesicles. *Biochim. Biophys. Acta* **1241**, 269–292 (1995).
41. B. Klasczyk, V. Knecht, R. Lipowsky, R. Dimova, Interactions of alkali metal chlorides with phosphatidylcholine vesicles. *Langmuir* **26**, 18951–18958 (2010).
42. T. P. Tuyen Dao *et al.*, Phase separation and nanodomain formation in hybrid polymer/lipid vesicles. *ACS Macro Lett.* **4**, 182–186 (2015).
43. S. Chakraborty *et al.*, How cholesterol stiffens unsaturated lipid membranes. *Proc. Natl. Acad. Sci. U.S.A.* **117**, 21896–21905 (2020).
44. L. A. Bagatolli, To see or not to see: Lateral organization of biological membranes and fluorescence microscopy. *Biochim. Biophys. Acta* **1758**, 1541–1556 (2006).
45. H.-J. Kaiser *et al.*, Order of lipid phases in model and plasma membranes. *Proc. Natl. Acad. Sci. U.S.A.* **106**, 16645–16650 (2009).
46. E. Sezgin *et al.*, Adaptive lipid packing and bioactivity in membrane domains. *PLoS One* **10**, e0123930 (2015).
47. S. Ballweg *et al.*, Regulation of lipid saturation without sensing membrane fluidity. *Nat. Commun.* **11**, 756 (2020).
48. S. Hrafnadóttir, J. W. Nichols, A. K. Menon, Transbilayer movement of fluorescent phospholipids in Bacillus megaterium membrane vesicles. *Biochemistry* **36**, 4969–4978 (1997).
49. J. M. Gardner, C. F. Abrams, Lipid flip-flop vs. lateral diffusion in the relaxation of hemifusion diaphragms. *Biochim. Biophys. Acta Biomembr.* **1860**, 1452–1459 (2018).
50. K. Göpprich *et al.*, One-pot assembly of complex giant unilamellar vesicle-based synthetic cells. *ACS Synth. Biol.* **8**, 937–947 (2019).
51. I. Ivanov *et al.*, Directed growth of biomimetic microcompartments. *Adv. Biosyst.* **3**, e1800314 (2019).
52. X. Wang *et al.*, Chemical communication in spatially organized protocell colonies and protocell/living cell micro-arrays. *Chem. Sci. (Camb.)* **10**, 9446–9453 (2019).
53. P. Yang, R. Lipowsky, R. Dimova, Nanoparticle formation in giant vesicles: Synthesis in biomimetic compartments. *Small* **5**, 2033–2037 (2009).
54. O. Biner, J. G. Fedor, Z. Yin, J. Hirst, Bottom-up construction of a minimal system for cellular respiration and energy regeneration. *ACS Synth. Biol.* **9**, 1450–1459 (2020).
55. D. Marsh, Protein modulation of lipids, and vice-versa, in membranes. *Biochim. Biophys. Acta* **1778**, 1545–1575 (2008).
56. B. Oberfeld, J. Brunner, P. Dimroth, Phospholipids occupy the internal lumen of the c ring of the ATP synthase of Escherichia coli. *Biochemistry* **45**, 1841–1851 (2006).
57. S. Laage, Y. Tao, A. E. McDermott, Cardiolipin interaction with subunit c of ATP synthase: Solid-state NMR characterization. *Biochim. Biophys. Acta* **1848**, 260–265 (2015).
58. G. F. Ames, Lipids of Salmonella typhimurium and Escherichia coli: Structure and metabolism. *J. Bacteriol.* **95**, 833–843 (1968).
59. Z. Zhao *et al.*, Super-resolution imaging of highly curved membrane structures in giant vesicles encapsulating molecular condensates. *Adv. Mater.* **34**, e2106633 (2022).
60. P. L. Felgner *et al.*, Lipofection: A highly efficient, lipid-mediated DNA-transfection procedure. *Proc. Natl. Acad. Sci. U.S.A.* **84**, 7413–7417 (1987).
61. X. Gao, L. Huang, A novel cationic liposome reagent for efficient transfection of mammalian cells. *Biochem. Biophys. Res. Commun.* **179**, 280–285 (1991).
62. R. Leventis, J. R. Silvius, Interactions of mammalian cells with lipid dispersions containing novel metabolizable cationic amphiphiles. *Biochim. Biophys. Acta* **1023**, 124–132 (1990).
63. R. C. MacDonald, V. A. Rakhmanova, K. L. Choi, H. S. Rosenzweig, M. K. Lahiri, O-ethylphosphatidylcholine: A metabolizable cationic phospholipid which is a serum-compatible DNA transfection agent. *J. Pharm. Sci.* **88**, 896–904 (1999).
64. M. Hung, L. Huang, E. Wagner, *Nonviral Vectors for Gene Therapy* (Springer, 2001).



## **Supplementary Information for**

Increased efficiency of charge-mediated fusion in polymer/lipid hybrid membranes

Nika Marušič<sup>†</sup>, Lado Otrin<sup>†</sup>, Jonas Rauchhaus<sup>†</sup>, Ziliang Zhao<sup>‡§#</sup>, Fotis L. Kyrilis<sup>||</sup>, Farzad Hamdi<sup>||</sup>, Panagiotis L. Kastiris<sup>||</sup>, Rumiana Dimova<sup>‡</sup>, Ivan Ivanov<sup>†\*</sup>, Kai Sundmacher<sup>†</sup>

<sup>†</sup>Process Systems Engineering, Max Planck Institute for Dynamics of Complex Technical Systems, Sandtorstraße 1, 39106 Magdeburg, Germany

<sup>‡</sup>Department of Theory and Bio-Systems, Max Planck Institute of Colloids and Interfaces, Science Park Golm, 14476 Potsdam, Germany

<sup>§</sup>Leibniz Institute of Photonic Technology e.V., 07745 Jena, Germany

<sup>#</sup>Faculty of Physics and Astronomy, Institute of Applied Optics and Biophysics, Friedrich Schiller University Jena, 07743 Jena, Germany

<sup>||</sup>Interdisciplinary Research Center HALOmem & Institute of Biochemistry and Biotechnology, Martin Luther University Halle-Wittenberg, Biozentrum, 06120 Halle/Saale, Germany

Email: ivanov@mpi-magdeburg.mpg.de

### **This PDF file includes:**

Supplementary text for Materials and Methods  
Figures S1 to S45  
SI References

## Supplementary Information Text for Materials and Methods

**Chemicals.** 1,2-dioleoyl-sn-glycero-3-phosphocholine (18:1 ( $\Delta^9$ -Cis) PC (DOPC)), L- $\alpha$ -phosphatidylserine (soy, 99%) (sodium salt) (soy PS), 1,2-dioleoyl-3-trimethylammonium-propane (chloride salt) (18:1 TAP (DOTAP)), 1,2-dioleoyl-sn-glycero-3-phosphoethanolamine-N-(7-nitro-2-1,3-benzoxadiazol-4-yl) (ammonium salt) (18:1 NBD PE), 1,2-dioleoyl-sn-glycero-3-phosphoethanolamine-N-(lissamine rhodamine B sulfonyl) (ammonium salt) (18:1 Liss Rho PE), L- $\alpha$ -Phosphatidylethanolamine-N-(lissamine rhodamine B sulfonyl) (ammonium salt) (egg-transphosphatidylated, chicken) (egg PE-Rho), 1-myristoyl-2-(6-[(7-nitro-2-1,3-benzoxadiazol-4-yl)amino]hexanoyl)-sn-glycero-3-phosphoethanolamine (14:0-06:0 NBD PE (M-NBD-PE)) and 1-myristoyl-2-(6-[(7-nitro-2-1,3-benzoxadiazol-4-yl)amino]hexanoyl)-sn-glycero-3-phosphocholine (14:0-06:0 NBD PC (M-NBD-PC)) were purchased from Avanti Polar Lipids. Succinimidyl ester (NHS)-rhodamine, NHS-fluorescein and Laurdan (6-dodecanoyl-2-dimethylaminonaphthalene) were purchased from Thermo Fisher Scientific. NHS-ATTO 514 was purchased from Merck. PDMS-*g*-PEO was a kind gift from Dow Corning. The viscosity-average molecular weight of 3000 g mol<sup>-1</sup>, the 47% weight fraction of ethylene oxide (2 arms of PEO per PDMS chain, on average) and the average degree of side chain polymerization of 12 and main chain polymerization of 26 are reported in the data provided by the supplier. PDMS-*g*-PEO labeled with fluorescein (PDMS-*g*-PEO-FITC) or rhodamine (PDMS-*g*-PEO-Rho) was synthesized following a previously described procedure (1) and was used as a fluorescent polymer marker for the visualization of hybrid membrane in fluorescent microscopy. The *E. coli* *bo*<sub>3</sub> oxidase was expressed from plasmid pETcyo in *E. coli* strain C43 (DE3)( $\Delta$ cyoABCDE) and purified as described (2). The *E. coli* F<sub>1</sub>F<sub>o</sub> ATP synthase was expressed from plasmid pBWU13- $\beta$ His in *E. coli* strain DK8 ( $\Delta$ uncBEFHAGDC) and purified as previously described (3).

**Preparation of LUVs for membrane mixing.** Liposomes were prepared from DOPC, DOPC/DOTAP (70–95:30–5, molar ratio) or DOPC/PS (70–95:30–5, molar ratio). Hybrids were prepared from PDMS-*g*-PEO/soy PS (70–95:30–5 molar ratio), PDMS-*g*-PEO/DOTAP (70–95:30–5 molar ratio) or PDMS-*g*-PEO/DOPC (90:10, molar ratio). Anionic liposomes and hybrids were supplemented with 0.5/1.5 mol% PE-Rho and 0.5/1.5 mol% PE-NBD. 5 mg of lipid/polymer mixture (for hybrids), or 5 mg of lipid (for liposomes) in chloroform/methanol (2:1, v/v) were deposited in a glass vial and the solvent was removed by evaporation under a gentle stream of nitrogen for ~30 min. The thin lipid or lipid/polymer film was rehydrated either with

200 mM sucrose, or with buffered solution (20 mM Tris (pH 8.0), 20 mM H<sub>3</sub>PO<sub>4</sub>) and resuspended to a final lipid concentration of 5 mg ml<sup>-1</sup> by vortexing. The suspension of multilamellar vesicles (MLVs) was subjected to 5 freeze-thaw cycles (1 min liquid nitrogen, then water bath at 35 °C until thawed completely, followed by 30 s vortexing). Finally, the size and lamellarity of vesicles was unified by extrusion (11 times) through a 100-nm pore (polycarbonate membrane, Avanti Mini Extruder).

**Determination of LUVs size and dispersity by dynamic light scattering (DLS).** Size and dispersity of (proteo)LUVs before and after fusion was determined by DLS. DLS experiments were performed using a Zetasizer Nano ZS (Malvern, Worcestershire, UK) with a 633 nm helium-neon laser with back-scattering detection. Undiluted (proteo)LUVs were measured at a fixed 173° scattering angle in a 45 µl-quartz cuvette. For each sample, two measurements of 10–100 runs were performed.

**Zeta potential measurements.** Zeta potential measurements were done with Zetasizer Nano ZS (Malvern, Worcestershire, UK). 900 µl of media was transferred with 1-ml glass syringe into a disposable folded capillary cell (DTS 1070). Next, 100 µl of vesicle suspension (60 mg ml<sup>-1</sup>) was transferred on the bottom of the cell and zeta potential was measured directly after. Zeta potential was measured with the following settings: model Smoluchowski, 23 °C, equilibration time 0 s, data processing auto mode. Each sample was measured three times (10–400 runs per measurement). Vesicles were measured in two different solutions: 200 mM sucrose and ATP synthase measurement buffer (20 mM Tris-PO<sub>4</sub> (pH 8.0)).

**Analysis of interbilayer and transbilayer transport of M-NBD-phospholipids.**

**Preparation of donor and acceptor LUVs.** Donor neutral lipid LUVs contained 3 mol% M-NBD-PE (or M-NBD-PC), 6 mol% Egg PE-Rho, and 91 mol% DOPC. Donor cationic or anionic lipid LUVs contained 3 mol% M-NBD-PE (or M-NBD-PC), 6 mol% egg PE-Rho, 10 mol% DOTAP or soy PS, and 81 mol% DOPC. Donor neutral hybrid LUVs contained 3 mol% M-NBD-PE (or M-NBD-PC), 6 mol% egg PE-Rho, 10 mol% DOPC, and 81 mol% PDMS-*g*-PEO. Donor cationic or anionic hybrid LUVs contained 3 mol% M-NBD-PE (or M-NBD-PC), 6 mol% egg PE-Rho, 10 mol% DOTAP or soy PS, and 81 mol% PDMS-*g*-PEO. Acceptor LUVs contained 100 or 90 mol% DOPC or PDMS-*g*-PEO, 0 or 10 mol% of anionic or cationic lipids, and no lipid dye. LUVs were prepared in 200 mM sucrose by freeze-thaw cycles and extrusion, as described above.

**Transport assay using fluorescent phospholipids.** To 1 ml of 200 mM sucrose (blank) in 1.5-ml quartz cuvette, 2.5 µl donor vesicles (0.8 mM lipid/polymer) were added and baseline was recorded in fluorescence

spectrophotometer Varian Cary Eclipse (Agilent) at excitation 460 nm and emission 533 nm for M-NBD-PE and at excitation 464 nm and emission 531 nm for M-NBD-PC (10/20 nm slit width) at constant stirring. To initiate the transport, 5  $\mu$ l acceptor vesicles (0.8 mM or 1.6 mM lipid/polymer) were added and fluorescence was monitored for ~6 min. Introduction of the acceptor vesicles prompted a sharp increase in fluorescence followed by a second slower increase (hybrids) or a plateau (liposomes). The fluorescence increase was fitted to single or double exponential equation. Rate constants,  $k_1$  and  $k_2$ , described the fast and the slow phase, respectively. Curve fitting was performed in Origin 2018.

### **Charge-mediated hybrid GUV-LUV and GUV-GUV fusion.**

**Preparation of anionic and cationic GUVs.** Hybrid and lipid GUVs were obtained with electroformation at room temperature. For anionic hybrids, 1 mg of PDMS-*g*-PEO/soy PS mixture (79.5:20, 69.92:30 or 69.5:29.7, mol%), containing 0.5 mol% PE-NBD (for GUV-LUV fusion), 0.08 mol% PDMS-*g*-PEO-Rho (for GUV-GUV fusion) or 0.3 mol% PE-Rho and 0.5 mol% PDMS-*g*-PEO-FITC (for lipid/polymer distribution analysis) was dissolved in 1 ml of 2:1 chloroform:methanol (v/v). For cationic hybrids, 1 mg of PDMS-*g*-PEO/DOTAP mixture (79.5:20, 69.1:30 or 69.5:30, mol%), containing 0.9 mol% PE-NBD or 0.5 mol% PDMS-*g*-PEO-FITC was dissolved in 1 ml of 2:1 chloroform:methanol (v/v). For cationic liposomes 1 mg of DOPC/DOTAP mixture (69.6:30, mol%), containing 0.4 mol% PE-NBD was dissolved in 1 ml of 2:1 chloroform:methanol (v/v). For neutral hybrids 1 mg of PDMS-*g*-PEO/DOPC mixture (79.5:20, 69.1:30 or 69.5:30, mol%), containing 0.5 or 0.9 mol% PE-NBD was dissolved in 1 ml of 2:1 chloroform:methanol (v/v). 25  $\mu$ l of those solutions were spread on each of both glass slides of a homemade electroformation device composed of two electrodes (glass slides coated with indium tin oxide with resistivity of 55  $\Omega$ ) and a silicone spacer (1.81 mm thick). Solvent was evaporated under a gentle stream of nitrogen and the electroformation chamber was filled with 200 mM sucrose. A sine wave at 1.6 V, 10 Hz was applied for 8 h, followed by detachment step at 2 V, 4 Hz for 30 min.

**Preparation of hybrid LUVs.** Hybrid LUVs (5 mg ml<sup>-1</sup>) in 200 mM sucrose were prepared by freeze-thaw and extrusion (200 nm) from PDMS-*g*-PEO/DOTAP/PE-Rho mixture or PDMS-*g*-PEO/DOPC/PE-Rho mixture at molar ratio of 79.5:20:0.5.

### **Functional coupling of *bo*<sub>3</sub> oxidase and F<sub>1</sub>F<sub>o</sub>-ATPase.**

**Vesicle preparation.** Liposomes were prepared from DOPC, DOPC/soy PS (70:30, molar ratio) or DOPC/DOTAP (70:30, molar ratio), hybrids were prepared from PDMS-*g*-PEO/DOPC, PDMS-*g*-PEO/soy PS or PDMS-*g*-PEO/DOTAP (all at 70:30, molar ratio). 10 mg of lipid (liposomes) or 30 mg of lipid/polymer mixture (for hybrids) in chloroform:methanol (2:1, v/v) were deposited in a glass vial and the solvent was removed by evaporation under a gentle stream of nitrogen for ~30 min. The thin lipid or lipid/polymer film was rehydrated with 20 mM Tris-phosphate buffer (pH 8.0) and resuspended to a final lipid concentration of 10 mg ml<sup>-1</sup> (liposomes) or lipid/polymer concentration of 30 mg ml<sup>-1</sup> (hybrids) by vortexing. The suspension of multilamellar vesicles (MLVs) was subjected to 5 freeze-thaw cycles (1 min liquid nitrogen, then water bath at 35 °C until thawed completely, followed by 30 s vortexing). Finally, the size and lamellarity of vesicles was unified by extrusion (21 times) through a 100 nm pore (polycarbonate membrane, Avanti Mini Extruder).

**Vesicles solubilization.** Solubilization of 100 nm vesicles upon step-wise addition of detergent was monitored via absorbance at 540 nm. First, 100 µl hybrids (30 mg ml<sup>-1</sup>) or 100 µl liposomes (10 mg ml<sup>-1</sup>) in 20 mM Tris-PO<sub>4</sub> (pH 8.0) was transferred into 100-µl quartz cuvette and initial absorbance was measured. Next, sodium cholate, sodium deoxycholate or Triton X-100 was added to the vesicles, followed by 1-min incubation at room temperature and absorbance measurement. The step was repeated 30–40 times until vesicles were completely solubilized. Vesicles size distribution was analyzed by DLS before solubilization, at saturation point ( $R_{\text{sat}}$ ) and at solubilization point ( $R_{\text{sol}}$ ).

**Reconstitution of *bo*<sub>3</sub> oxidase and F<sub>1</sub>F<sub>o</sub>-ATPase.** To achieve this same molar ratio of lipid/polymer-to-protein and at the same time the same molar concentration of proteins in reconstitution mixture, we reconstituted both proteins in 10 mg ml<sup>-1</sup> liposomes and 30 mg ml<sup>-1</sup> hybrids. For reconstitution of *bo*<sub>3</sub> oxidase Triton-X 100 was added to DOPC/DOTAP or DOPC liposomes (10 mg ml<sup>-1</sup> LUVs, final conc. of Triton X-100 corresponded to  $R_{\text{sat}}$ ) or sodium cholate to PDMS-*g*-PEO/DOTAP or PDMS-*g*-PEO/DOPC hybrids (30 mg ml<sup>-1</sup> LUVs, final conc. of sodium cholate corresponded to  $R_{\text{sat}}$ ). For reconstitution of F<sub>1</sub>F<sub>o</sub>-ATPase sodium deoxycholate was added to DOPC/soy PS or DOPC liposomes (10 mg ml<sup>-1</sup> LUVs, final conc. of sodium deoxycholate corresponded to  $R_{\text{sat}}$ ) and to PDMS-*g*-PEO/soy PS or PDMS-*g*-PEO/DOPC hybrids (30 mg ml<sup>-1</sup> LUVs, final conc. of sodium deoxycholate corresponded to  $R_{\text{sol}}$ ). Next, *bo*<sub>3</sub> oxidase or

F<sub>1</sub>F<sub>0</sub>-ATPase was gently added to the vesicles at final conc. of 0.42  $\mu$ M and 0.14  $\mu$ M, respectively. The reconstitution mixture was incubated at 4 °C for 30 min with mild agitation, followed by detergent removal via Bio-Beads SN-2 (Bio-Rad). For preparation of proteoliposomes, for 100  $\mu$ l of reconstitution mixture 45 mg was added at once and incubated for 1.5 h at room temperature, on a rocking platform. Meanwhile, for preparation of 100  $\mu$ l of proteohybrids suspension, the beads were added in 3 subsequent additions, 15 mg of beads each, followed by 30 min incubation period, at room temperature, on a rocking platform. After that, beads were pelleted and the supernatant (proteovesicles) was collected and stored on 4 °C.

**Respiratory-driven ATP synthesis measurements.** Measurements of respiration-driven ATP production were performed as described previously (4), with slight modification. To a solution containing 112.8  $\mu$ l of measurement buffer (20 mM Tris-phosphate (pH 8.0), 2.26  $\mu$ l of luciferin/luciferase assay (CLSII, prepared according to manufactures protocol) and 5.4  $\mu$ l of ADP (6.96 mM stock, ultra-pure), 2.26  $\mu$ l of proteoLUVs were added and a baseline was recorded. Next, 2.26  $\mu$ l of ATP (2  $\mu$ M stock) was added to normalize the signal against a defined ATP amount. The reaction was started by the addition of 1.5  $\mu$ l of DTT/Q<sub>1</sub> (prepared from 6  $\mu$ l 1 M DTT and 0.25  $\mu$ l 80 mM Q<sub>1</sub>) and synthesis of ATP was recorded. The ATP production rates were reported as the average of 2 separate reconstitutions (each measured in 4 replicates), with standard deviation.

#### **Delivery of bo<sub>3</sub> oxidase into hybrid GUVs.**

**Preparation of lipid and hybrid LUVs.** 100 nm LUVs were prepared via freeze-thaw and extrusion as described above. Lipid LUVs composition was DOPC:DOTAP (70:30, mol%) and hybrid LUVs composition was PDMS-*g*-PEO:DOTAP (70:30, mol%).

**Labeling of bo<sub>3</sub> oxidase.** Labeling with ATTO 425 NHS was done as described previously (5). The degree of labeling was determined to be 2.83 molecules of dye per enzyme.

**Reconstitution of bo<sub>3</sub> oxidase into cationic LUVs.** bo<sub>3</sub> oxidase-ATTO 425 was reconstituted into cationic lipid (10 mg ml<sup>-1</sup>) and hybrid (30 mg ml<sup>-1</sup>) LUVs at lipid/polymer molar ratio of 8000:1. For reconstitution into lipid LUVs 0.348 % Triton X-100 (saturation point, R<sub>sat</sub>) and for reconstitution into hybrid LUVs 0.074 % sodium cholate (R<sub>sat</sub>) was used.

**Preparation of anionic GUVs.** GUVs were prepared by electroformation as described above. To increase GUVs yield, electroformation chamber was placed in the oven at 50 °C.

**Wafer and microfluidic chip preparation.** Wafer and chips were prepared as described previously (5). Chips were coated with 2 % (w/v) bovine serum albumin (BSA) solution as described previously (5).

### **Cryo-TEM**

Cryo-TEM was performed on different hybrid LUVs in 200 mM sucrose and 20 mM Tris-PO<sub>4</sub> (pH 8.0): PDMS-*g*-PEO/DOTAP (70:30, mol%), PDMS-*g*-PEO/soy PS/PE-Rho/PE-NBD (69:30:0.5:0.5, mol%), PDMS-*g*-PEO/DOTAP (95:5, mol%), PDMS-*g*-PEO/soy PS/PE-Rho/PE-NBD (94:5:0.5:0.5, mol%), after fusion and in 20 mM Tris-PO<sub>4</sub> (pH 8.0): PDMS-*g*-PEO/DOTAP (70:30, mol%), PDMS-*g*-PEO/soy PS/PE-Rho/PE-NBD (69:30:0.5:0.5, mol%). The vitrification of the samples and image acquisition was performed as in ref. (5).

## Lipid dyes distribution in anionic hybrid GUVs

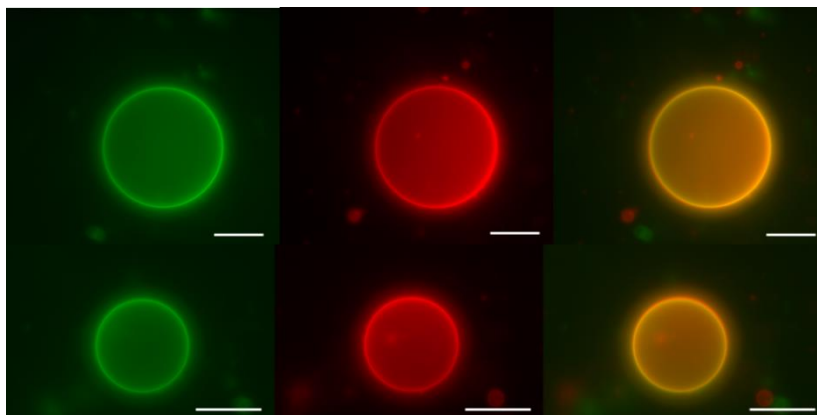


**Fig. S1.** Micrographs of hybrid GUVs (PDMS-*g*-PEO:soy PS:PE-Rho:PE-NBD = 89:10:0.5:0.5). Channels from left to right: NBD (green), Rhodamine (red) and merged. Scale bar: 10  $\mu$ m.

## Membrane mixing of LUVs

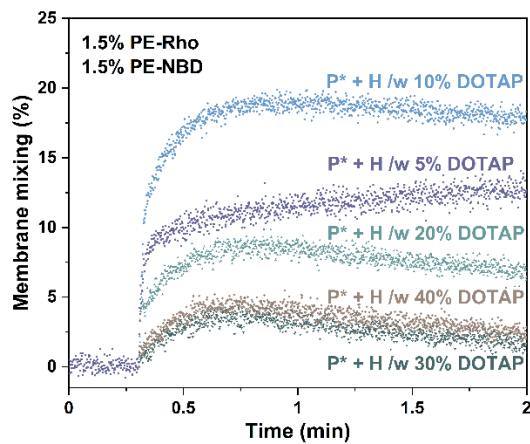


**Fig. S2.** Membrane mixing of  $\sim 100$  nm PDMS-*g*-PEO LUVs ("P\*"), containing 1.5 mol% PE-Rho and 1.5 mol% PE-NBD, and  $\sim 100$  nm hybrid LUVs ("H"), containing different amount of cationic lipids (0–40 mol%), mixed in molar ratio 1:1.

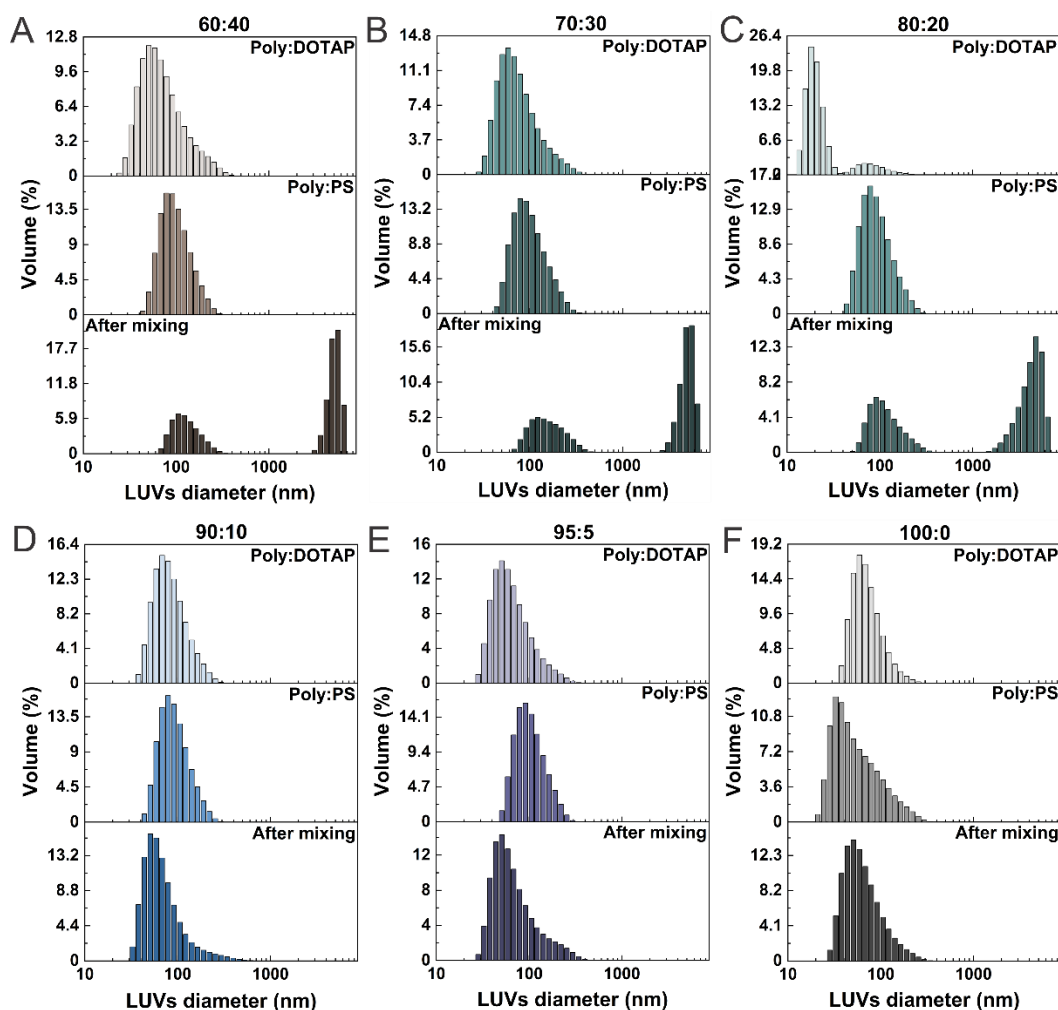


**Fig. S3.** Size of hybrid LUVs with different amount of charged lipids (from FRET experiment). Size distribution by volume of PDMS-*g*-PEO:DOTAP, PDMS-*g*-PEO:PS and PDMS-*g*-PEO LUVs before and after mixing (10 min at 500 rpm), determined by DLS. LUVs were composed of 40 (A), 30 (B), 20 (C), 10 (D), 5 (E) or 0 mol% charged lipids (F). LUVs containing PS were supplemented with 1.5 mol% PE-NBD and 1.5 mol% PE-Rho.

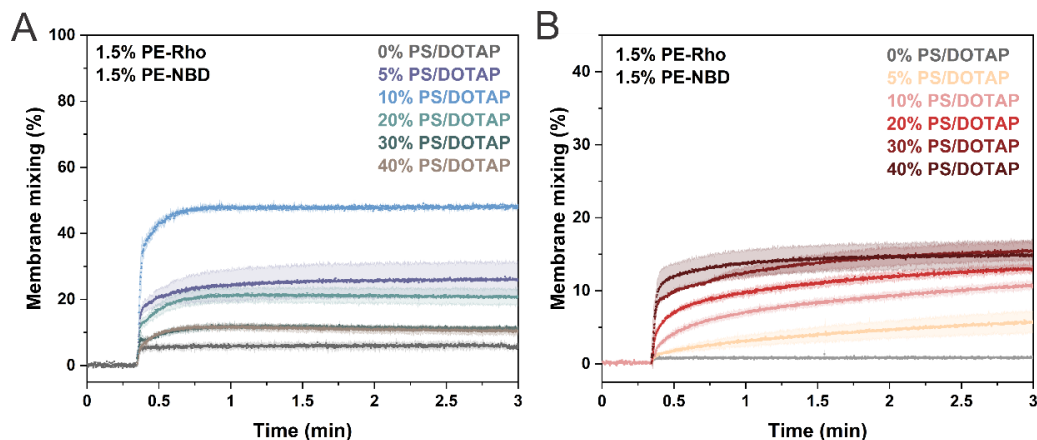


**Fig. S4.** Charge-mediated membrane mixing of hybrid (A) and lipid (B) LUVs with different amount of charged lipids. Tagged hybrids contained 1.5 mol% PE-Rho and 1.5 mol% PE-NBD. 100 % was obtained by solubilizing LUVs with Triton X-100. Error bars represent SD from  $n = 3$ .

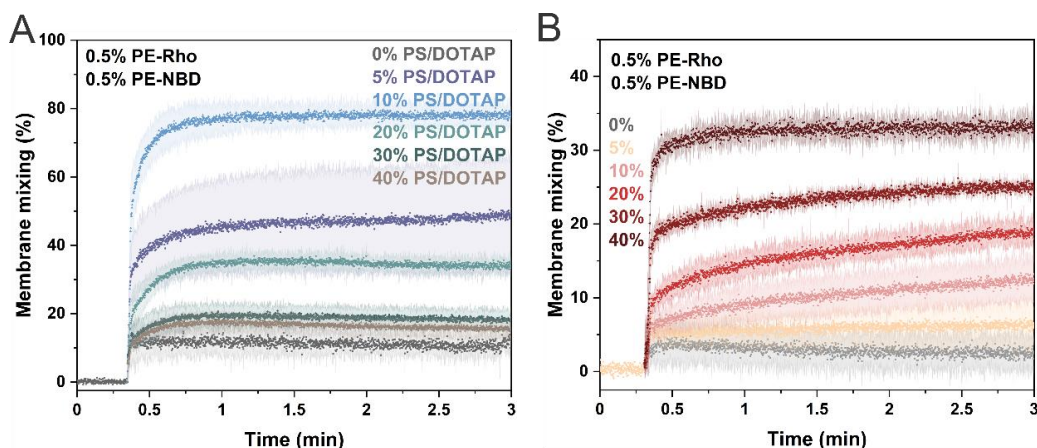


**Fig. S5.** Charge-mediated membrane mixing of hybrid (A) and lipid (B) LUVs with different amount of charged lipids. Tagged LUVs contained 0.5 mol% PE-Rho and 0.5 mol% PE-NBD. 100 % was obtained by solubilizing LUVs with Triton X-100. Error bars represent SD from  $n = 3$ .

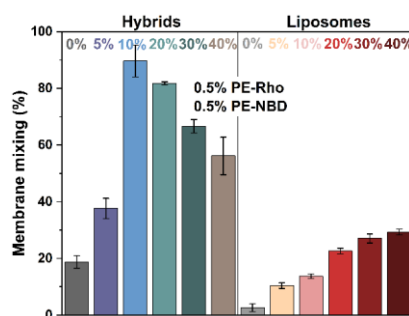


**Fig. S6.** Charge-mediated membrane mixing of lipid and hybrid LUVs with different amount of charged lipids. Hybrid LUVs were composed of 60–100 mol% PDMS-*g*-PEO and 0–40 mol% DOTAP or soy PS, and lipid LUVs of 60–100 mol% DOPC and 0–40 mol% DOTAP or soy PS. Anionic and cationic LUVs were mixed in molar ratio 1:1; final concentration of LUVs was 100  $\mu$ M. Anionic LUVs (DOPC:soy PS) were tagged with 0.5 mol% PE-Rho and 0.5 mol% PE-NBD. 100 % was obtained by solubilizing LUVs with octyl glucoside. Corresponding membrane mixing over time is shown in Fig. S7.

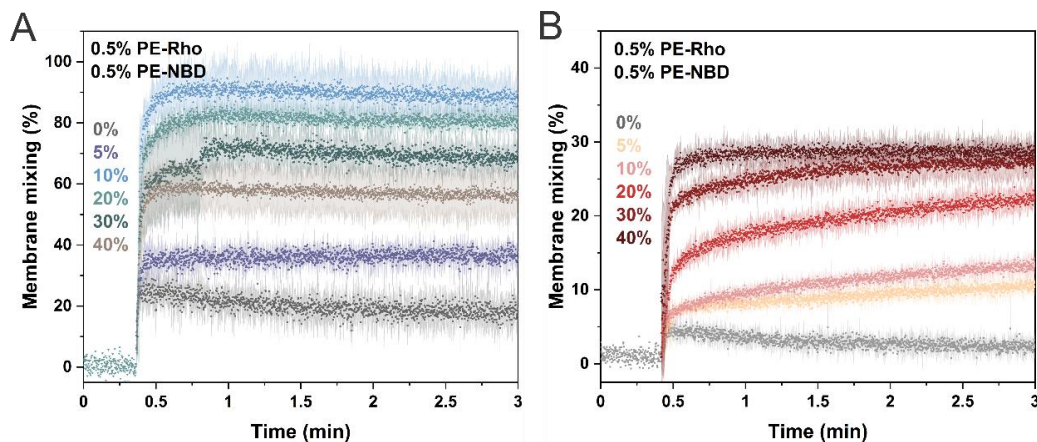


**Fig. S7.** Charge-mediated membrane mixing of hybrid and lipid LUVs with different amount of charged lipids. LUVs were composed of 60–100 mol% PDMS-*g*-PEO and 0–40 mol% DOTAP or soy PS. Anionic and cationic LUVs were mixed in molar ratio 1:1; final concentration of LUVs was 100  $\mu$ M. (A) Membrane mixing of  $\sim$  100 nm hybrid LUVs. Anionic LUVs (PDMS-*g*-PEO:soy PS) were tagged with 0.5 mol% PE-Rho and 0.5 mol% PE-NBD. 100 % was obtained by solubilizing LUVs with octyl glucoside. (B) Membrane mixing of  $\sim$  100 nm lipid LUVs. Anionic LUVs (DOPC:soy PS) were tagged with 0.5 mol% PE-Rho and 0.5 mol% PE-NBD. 100 % was obtained by solubilizing LUVs with octyl glucoside. Error bars represent SD from  $n = 3$ .

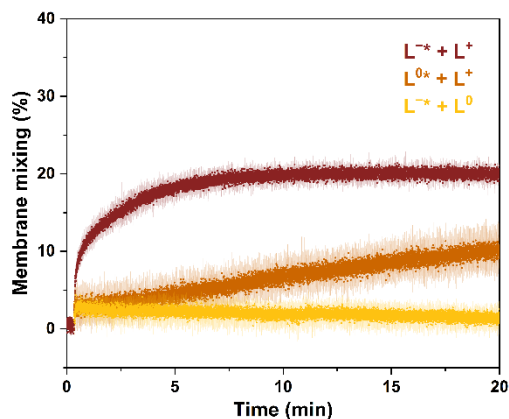


**Fig. S8.** Membrane mixing of  $\sim$  100 nm lipid LUVs in 200 mM sucrose over 20 min. Membrane mixing of neutral and cationic lipid LUVs increasing with slow rate can be observed. Asterisk indicates tagged (containing 0.5 mol% PE-Rho and 0.5 mol% PE-NBD) lipid LUVs. Error bars represent SD from  $n = 3$ .

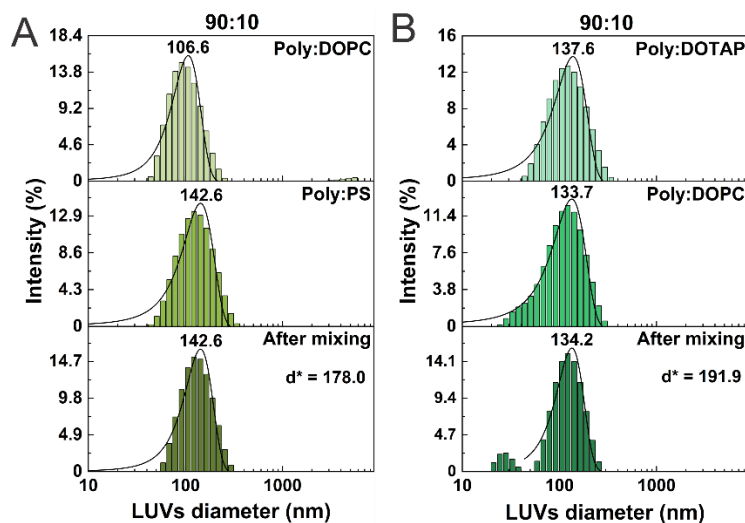


**Fig. S9.** Size distribution by intensity of neutral and charged hybrid LUVs (from FRET experiment) determined by DLS. LUVs in middle panel were supplemented with 0.5 mol% PE-NBD and 0.5 mol% PE-Rho. (A) Neutral and anionic hybrid LUVs. (B) Cationic and neutral hybrid LUVs.

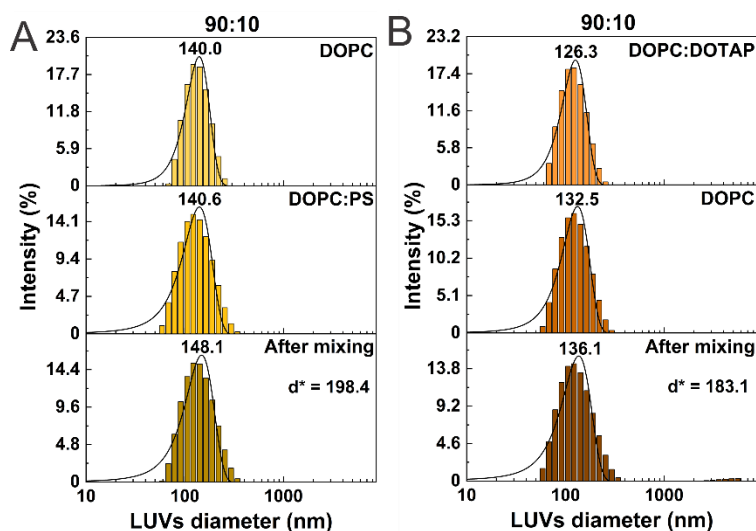


**Fig. S10.** Size distribution by intensity of neutral and charged lipid LUVs (from FRET experiment) determined by DLS. LUVs in middle panel were supplemented with 0.5 mol% PE-NBD and 0.5 mol% PE-Rho. (A) Neutral and anionic lipid LUVs. (B) Cationic and neutral lipid LUVs.  $d^*$  denotes expected mean diameter.

## Membrane thickness

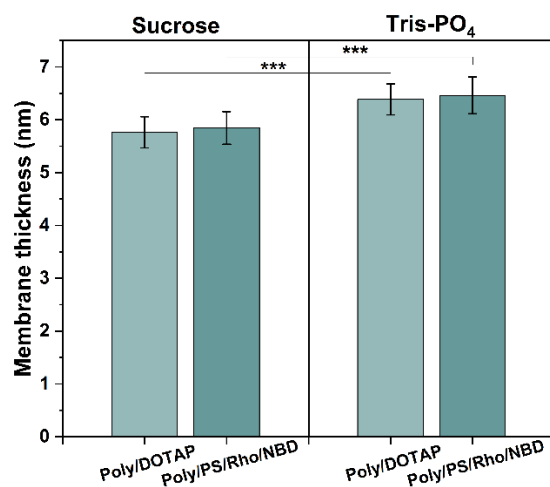


**Fig. S11.** Membrane thickness of hybrid LUVs in 200 mM sucrose and 20 mM Tris-PO<sub>4</sub> (pH 8.0). Hybrids were composed of 70 mol% PDMS-*g*-PEO and 30 mol% DOTAP or 69 mol% PDMS-*g*-PEO, 30 mol% soy PS, 0.5 mol% PE-Rho and 0.5 mol% PE-NBD. Error bars represent SD from  $n = 100$ . \*\*\* $P \leq 0.001$ .

## Membrane disorder

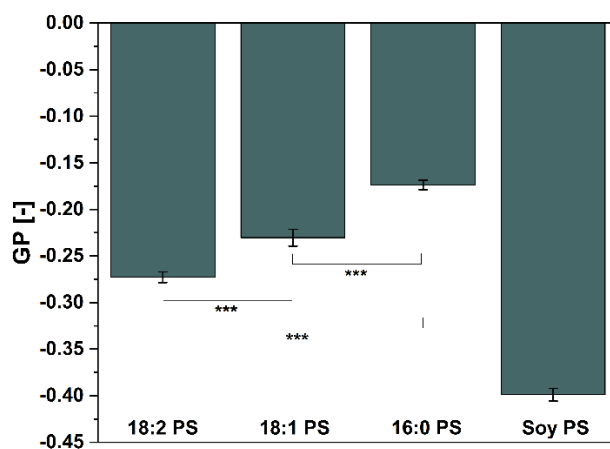


**Fig. S12.** Membrane disorder of hybrid LUVs. Generalized polarization (GP) values of hybrid LUVs with 70 mol% PDMS-*g*-PEO and 30 mol% 18:2 PS, 18:1 PS, 16:0 PS or soy PS in 200 mM sucrose. Soy PS contains 68% 18:2 PS, 12% 18:1 PS, 10% 16:0 PS, 7% 18:3 and 3% 18:0, as stated by manufacturer. Error bars represent SD from  $n = 4$ . \*\*\* $P \leq 0.001$ .

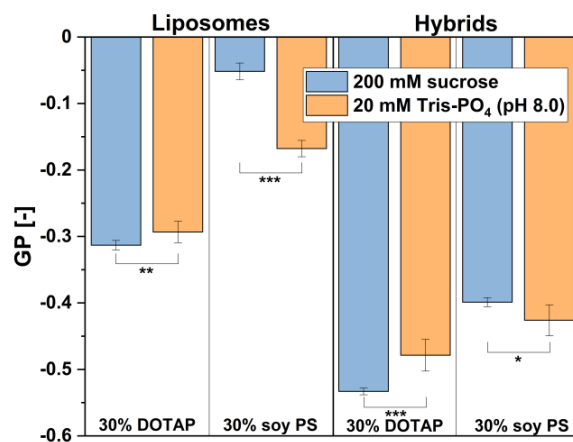


**Fig. S13.** Membrane disorder of lipid and hybrid LUVs. Generalized polarization (GP) values of lipid and hybrid LUVs with 30 mol% anionic (PS) or cationic (DOTAP) lipids in 200 mM sucrose (blue) and in 20 mM Tris-PO<sub>4</sub> (pH 8.0) (orange). Error bars represent SD from n = 3–6. \**P* ≤ 0.05; \*\**P* ≤ 0.01; \*\*\**P* ≤ 0.001.

#### Interbilayer and transbilayer transport of M-NBD-phospholipids

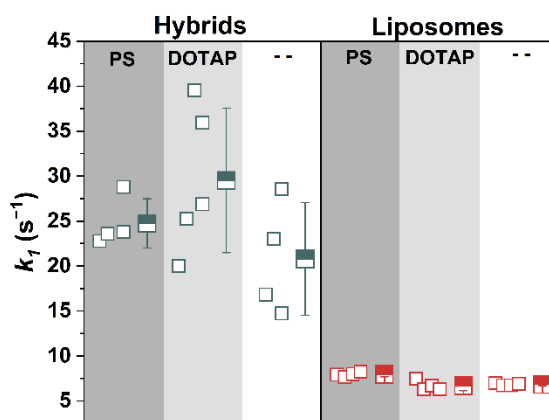


**Fig. S14.** Interbilayer transport of M-NBD-PE. The values correspond to a donor/acceptor polymer/lipid molar ratio of 0.5. Experimental data was fitted by single (for liposomes and some hybrids) or double (hybrids) exponential equation.

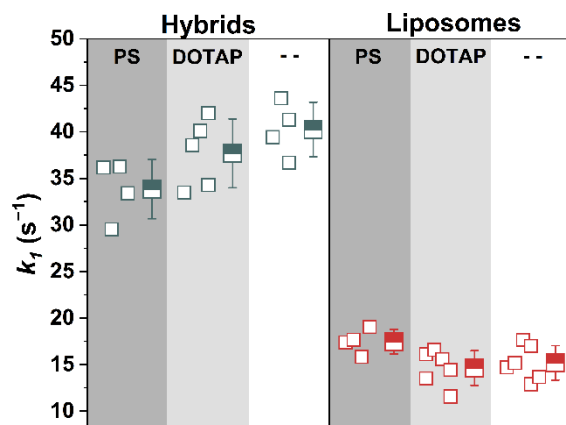


**Fig. S15.** Interbilayer transport of M-NBD-PC. The values correspond to a donor/acceptor polymer/lipid molar ratio of 0.25. Experimental data was fitted by single exponential equation.

### Hybrid GUV-LUV fusion

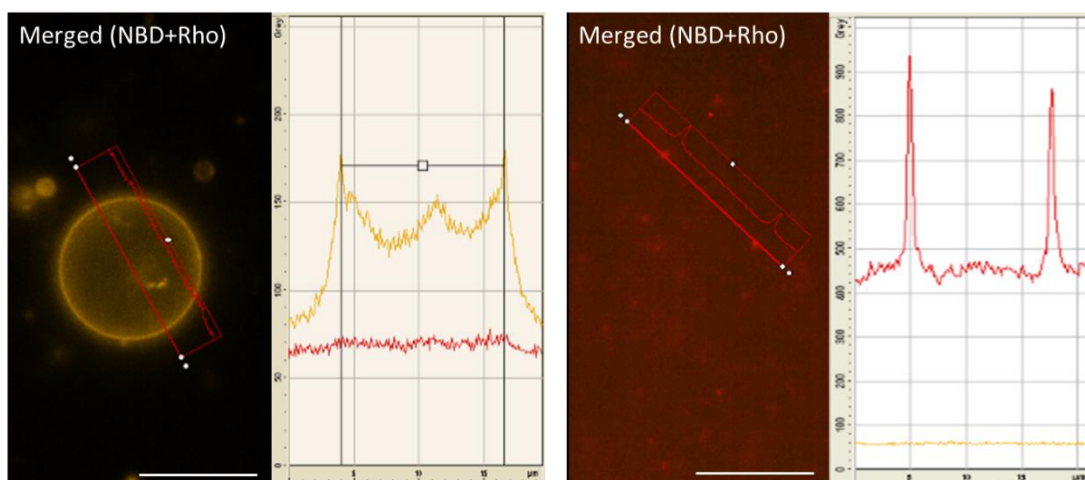


**Fig. S16.** Micrographs of NBD-GUVs (left) and Rho-LUVs (right). PDMS-*g*-PEO:PS (70:30, mol%) GUVs were labeled with PE-NBD (yellow). PDMS-*g*-PEO:DOTAP (70:30, mol%) LUVs were labeled with PE-Rho (red). Scale bar: 10  $\mu\text{m}$ .

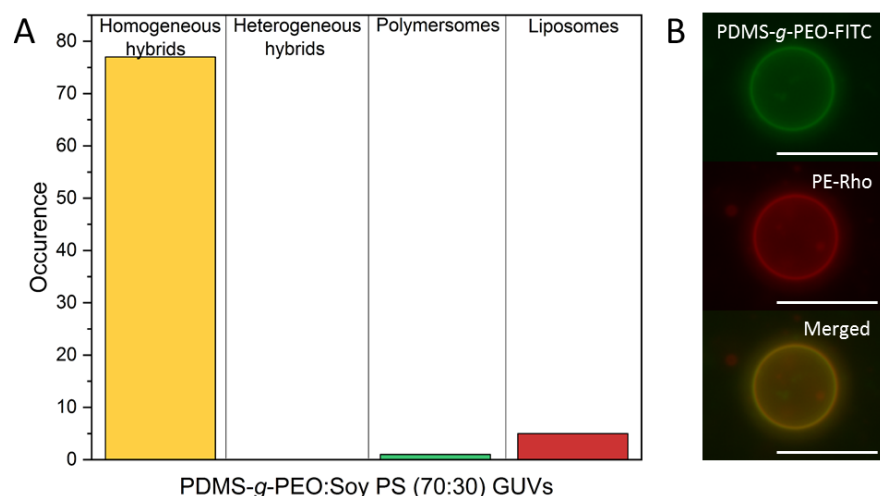


**Fig. S17.** Analysis of phase separation in anionic hybrid GUVs. Hybrids were made by electroformation from PDMS-*g*-PEO:soy PS:PE-Rho:PDMS-*g*-PEO-FITC (69.5:29.7:0.3:0.5). The presence of two membrane dyes reduced yield and size of GUV (in comparison when only one dye was used); majority of GUVs had diameter 4–5  $\mu\text{m}$ . Large majority of GUVs had homogenous distribution. GUVs were evaluated directly after formation. (A) Number of GUVs with homogeneous and heterogeneous lipid and polymer distribution, and number of GUVs containing only lipid or only polymer. (B) Example of homogenous lipid (red) and polymer (green) distribution in hybrid GUV. Scale bar: 10  $\mu\text{m}$ .

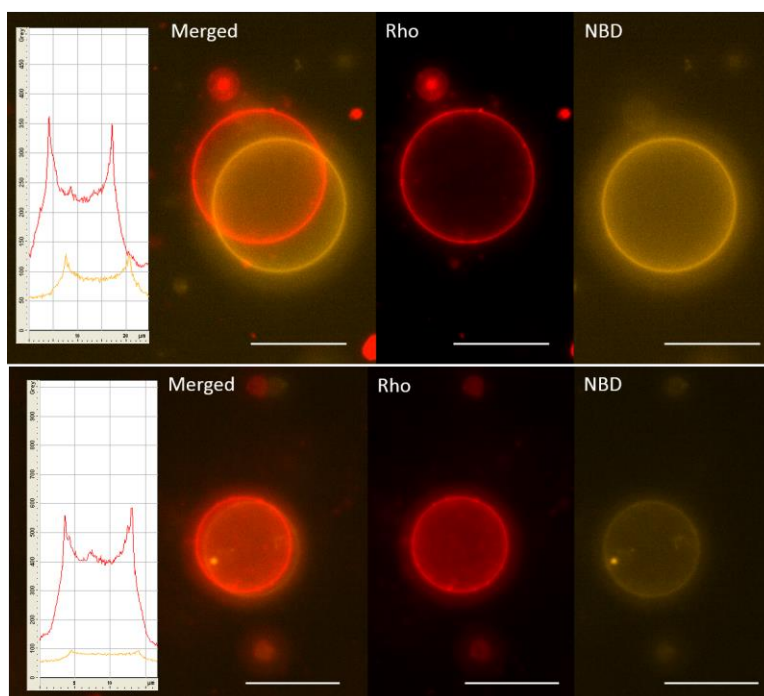


**Fig. S18.** Micrographs of PDMS-*g*-PEO:PS GUVs, tagged with PE-NBD (yellow), upon incubation with PDMS-*g*-PEO:DOTAP LUVs, tagged with PE-Rho (red). Both GUVs and LUVs were prepared in 200 mM sucrose. After incubation of Rho-LUVs with NBD-GUVs at 500 rpm for 10 min, both membrane dyes were observed in the membrane of GUVs. Scale bar: 10  $\mu\text{m}$ .

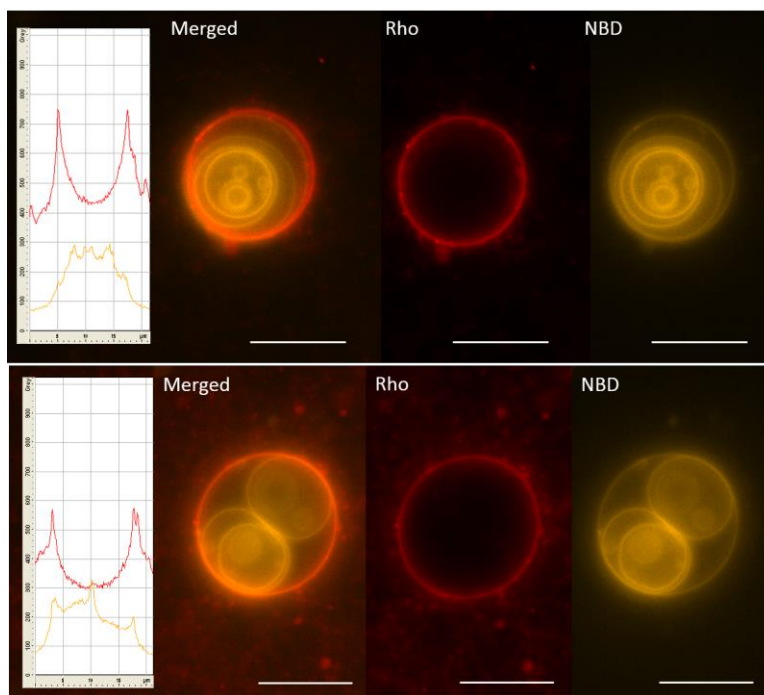


**Fig. S19.** Micrographs of multivesicular PDMS-*g*-PEO:PS GUV, tagged with PE-NBD (yellow), upon incubation with PDMS-*g*-PEO:DOTAP LUVs, tagged with PE-Rho (red). Both GUVs and LUVs were prepared in 200 mM sucrose. After incubation of Rho-LUVs with NBD-GUVs at 500 rpm for 10 min, both membrane dyes were observed in the membrane of GUVs. A portion of hybrid GUVs was multivesicular; in those vesicles, Rho-LUVs fused only with outer membrane. Scale bar: 10  $\mu$ m.

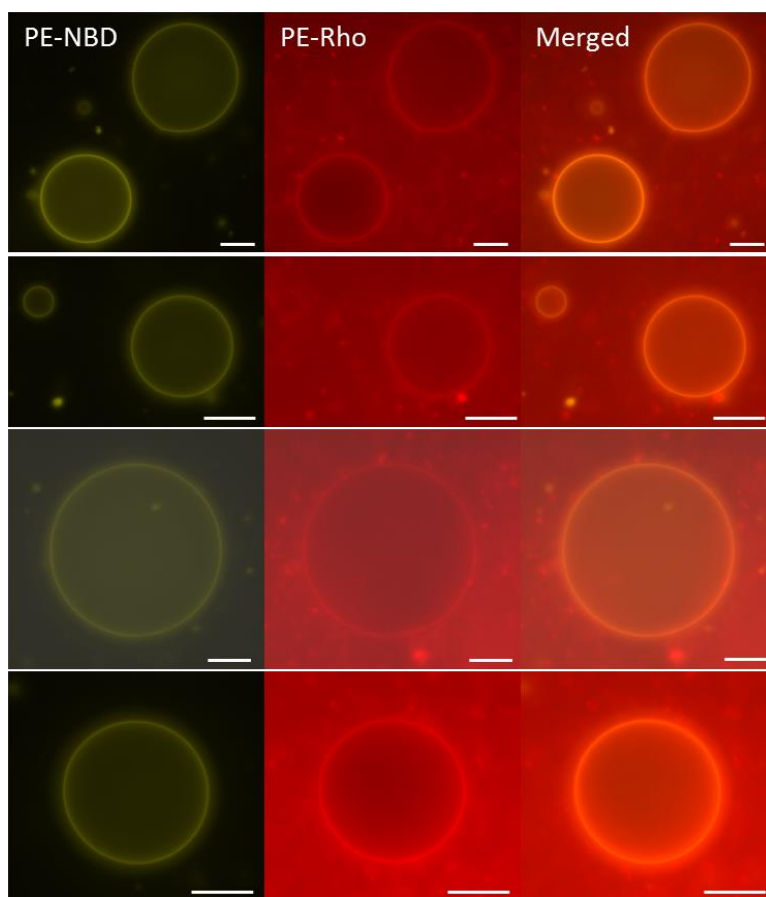


**Fig. S20.** Fluorescent microscopy of neutral GUVs (PDMS-*g*-PEO:DOPC:PE-NBD = 79.5:20:0.5, mol%; yellow) and cationic LUVs (PDMS-*g*-PEO:DOTAP:PE-Rho = 79.5:20:0.5, mol%; red) upon their incubation for 5 min. Accumulation of red signal from LUVs was observed on the membrane of GUVs. Scale bar: 10  $\mu$ m.

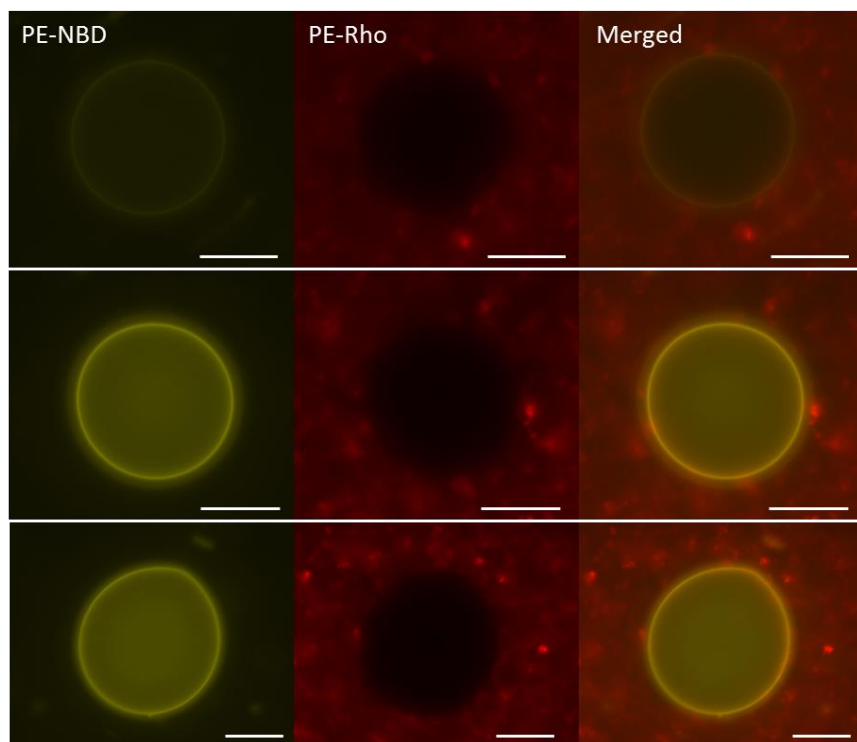


**Fig. S21.** Fluorescent microscopy of anionic GUVs (PDMS-*g*-PEO:soy PS:PE-NBD = 79.5:20:0.5, mol%; yellow) and neutral LUVs (PDMS-*g*-PEO:DOPC:PE-Rho = 79.5:20:0.5, mol%; red) upon their incubation for 5 min. No accumulation of red signal from LUVs on the GUVs was observed. Scale bar: 10  $\mu$ m.

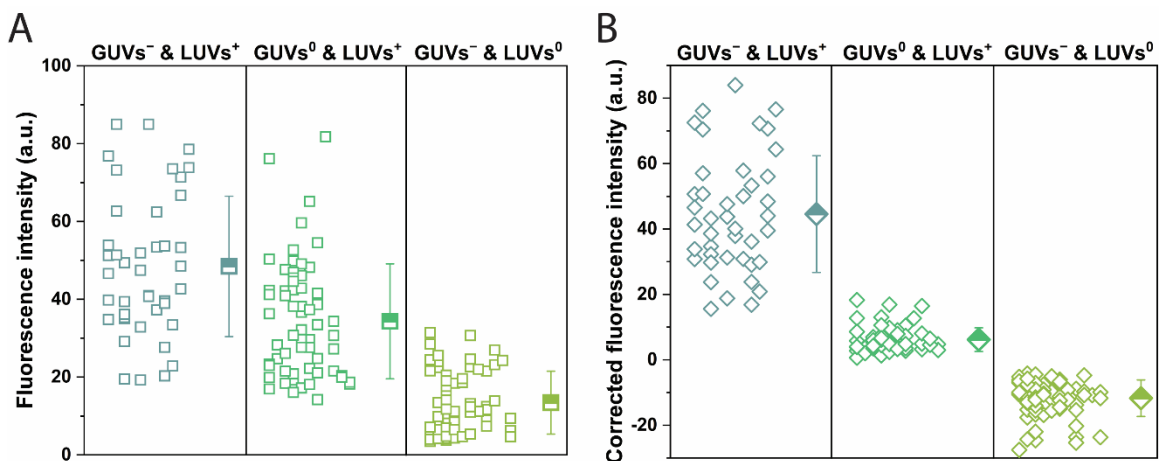


**Fig. S22.** PE-Rho fluorescence intensity on hybrid GUVs membrane after mixing with hybrid LUVs. GUVs contained 80 mol% of PDMS-*g*-PEO and 20 mol% soy PS or DOPC and were tagged with PE-NBD, LUVs contained 80 mol% of PDMS-*g*-PEO and 20 mol% DOTAP or DOPC and were tagged with PE-Rho (see Fig. S16–S19). Three setups were tested: mixing anionic GUVs with cationic LUVs (GUVs<sup>-</sup> & LUVs<sup>+</sup>), neutral GUVs with cationic LUVs (GUVs<sup>0</sup> & LUVs<sup>+</sup>) and anionic GUVs with neutral LUVs (GUVs<sup>-</sup> & LUVs<sup>0</sup>). (A) PE-Rho fluorescence intensity on the membrane of GUVs. (B) Corrected PE-Rho fluorescence intensity on the membrane of GUVs: from PE-Rho intensity on the membrane, PE-Rho signal in background was subtracted. PE-Rho intensity was analyzed from micrographs in ImageJ software.

## Hybrid GUV-GUV fusion

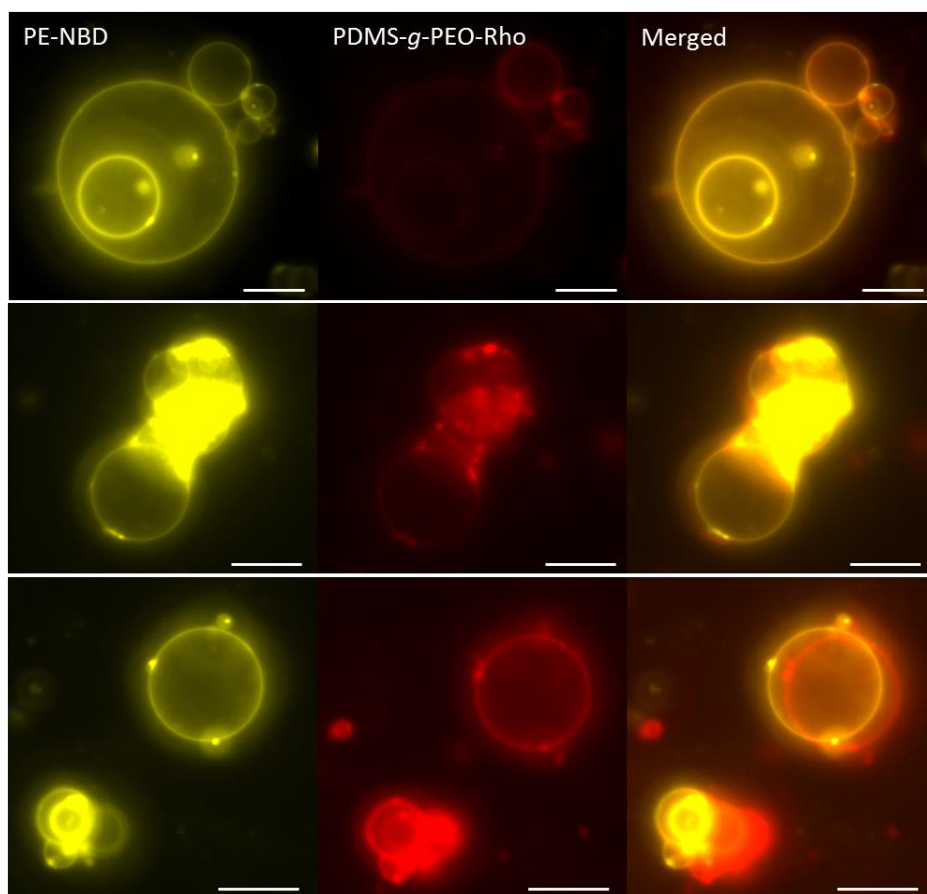


**Fig. S23.** Micrographs of hybrid GUVs upon fusion of anionic and cationic hybrid GUVs. Cationic GUVs were tagged with lipid dye (PDMS-*g*-PEO:DOTAP:PE-NBD (69.1:30:0.9); yellow) and anionic GUVs with polymer dye (PDMS-*g*-PEO:soy PS:PDMS-*g*-PEO-Rho (70:30:0.08); red). Aggregated PE-NBD observed on cationic hybrids alone (Fig. S23) was retained upon fusion with anionic hybrid GUVs. Difference in red and yellow signal indicates on asymmetric GUV-GUVs fusion in terms of their size. Scale bar: 10  $\mu\text{m}$ .

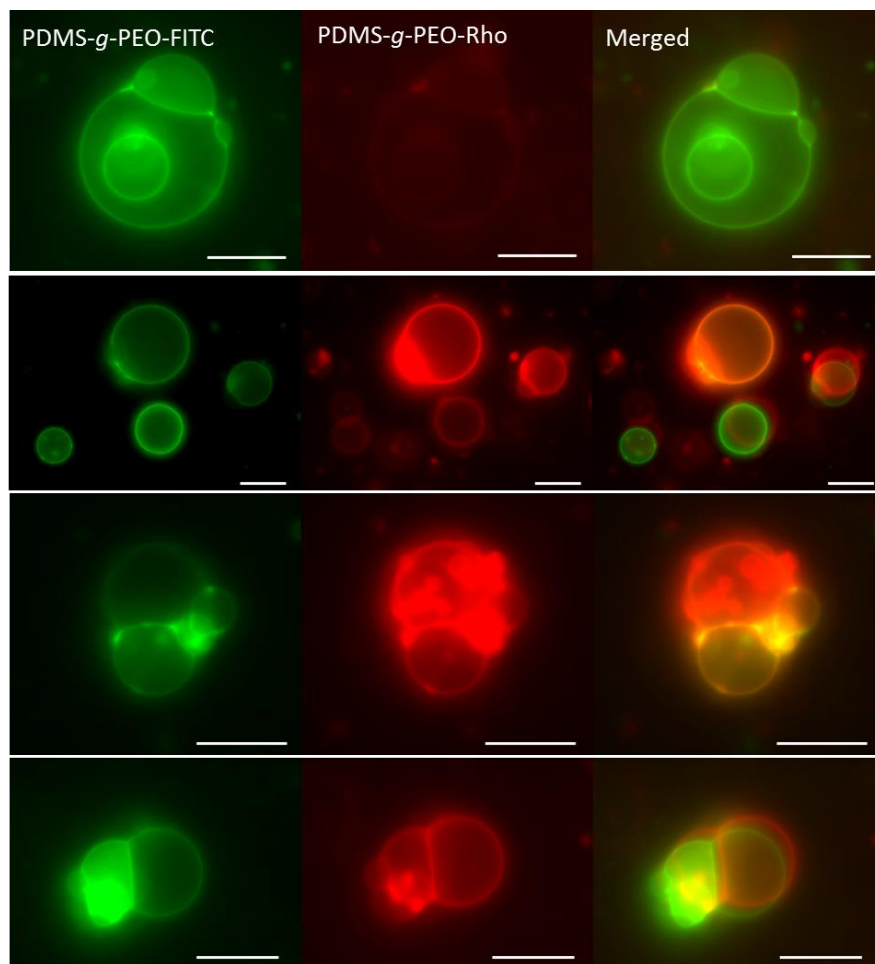


**Fig. S24.** Micrographs of hybrid GUVs upon fusion of cationic and anionic hybrid GUVs. Cationic and anionic hybrids were both tagged with polymer dyes: PDMS-*g*-PEO:DOTAP:PDMS-*g*-PEO-FITC (69.5:30:0.5) (green) and PDMS-*g*-PEO:soy PS:PDMS-*g*-PEO-Rho (70:30:0.08) (red), respectively. Due to absence of mixing and different GUVs size, the contribution of material from anionic and cationic GUVs varied in-between newly grown (fused) GUVs. Scale bar: 10  $\mu$ m.

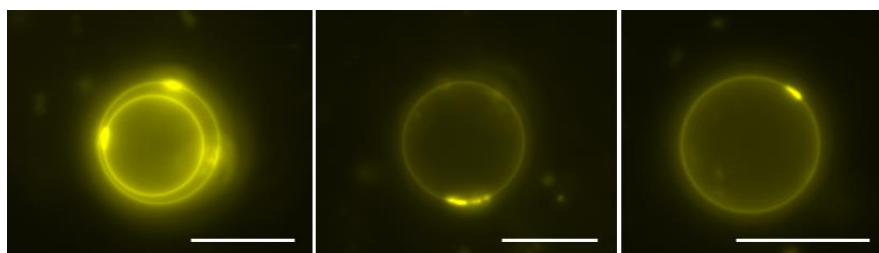


**Fig. S25.** Cationic hybrid GUVs with lipid dye (yellow). GUVs composition: PDMS-*g*-PEO:DOTAP:PE-NBD (69.1:30:0.9, mol%). In majority of GUVs PE-NBD aggregation was observed (strong yellow signal). Scale bar: 10  $\mu$ m.

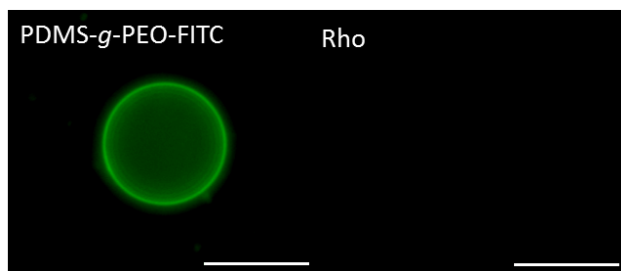


**Fig. S26.** Cationic hybrid GUVs with polymer dye (green). GUVs composition: PDMS-*g*-PEO:DOTAP:PDMS-*g*-PEO-FITC (69.5:30:0.5). No signal was observed with Rhodamine filter set. Opposite to GUVs labeled with PE-NBD (Fig. S23), no aggregation was observed here. Scale bar: 10  $\mu$ m.

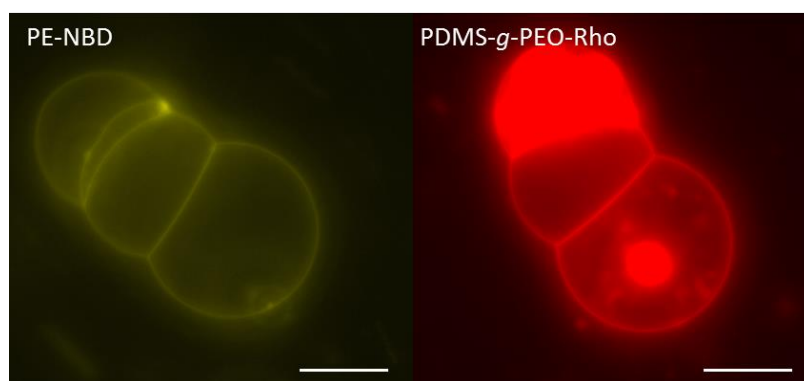


**Fig. S27.** Micrograph of hybrid GUVs after fusion of anionic (polymer-labeled, red) and cationic (lipid-labeled, yellow) hybrid GUV. Long contact between newly grown GUVs was often observed. Scale bar: 10  $\mu$ m.

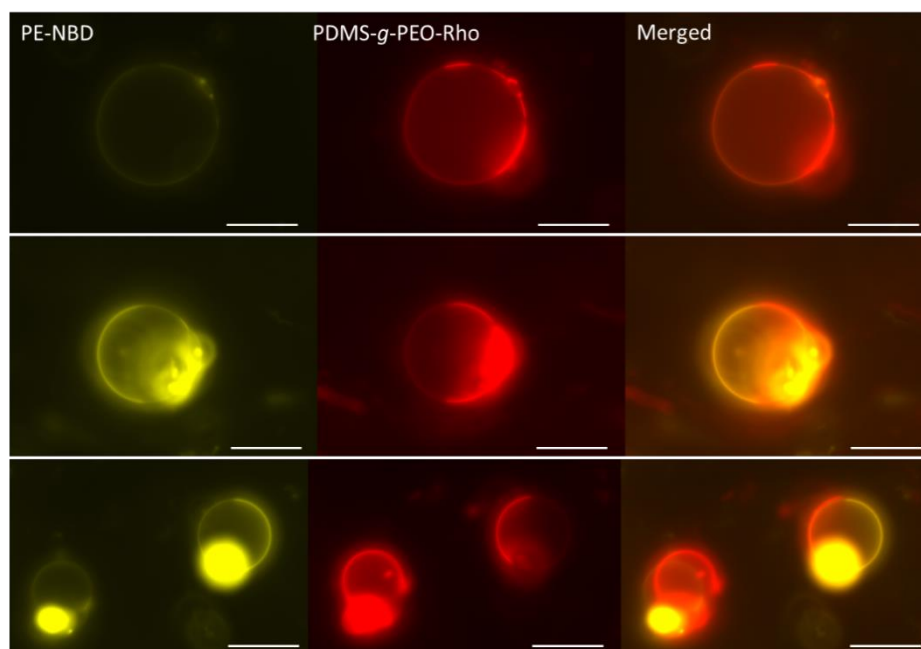


**Fig. S28.** Micrographs of heterogeneous (phase separated lipid and polymer domain) hybrid GUVs upon fusion of cationic lipid and anionic hybrid GUVs. Scale bar: 10  $\mu$ m.

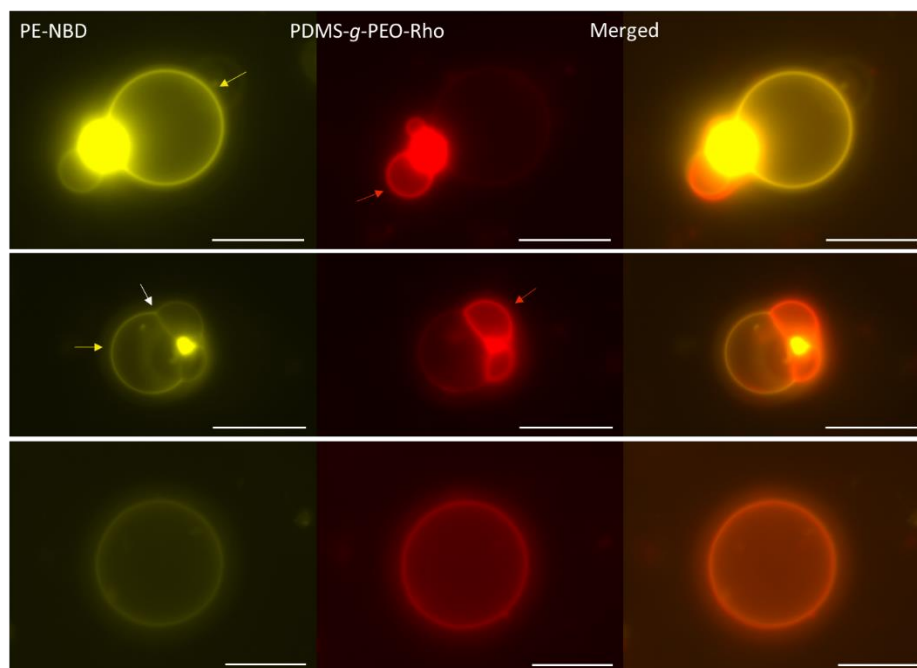


**Fig. S29.** Micrographs of homogenous hybrid GUVs upon fusion of cationic lipid and anionic hybrid GUVs. Yellow arrows indicate higher presence of lipid and red arrows higher presence of polymer. White arrows show long contacts between the two GUVs, where higher amount of polymer than lipid is present. Scale bar: 10  $\mu\text{m}$ .

### Functional coupling of $bo_3$ oxidase and $F_1F_0$ -ATPase

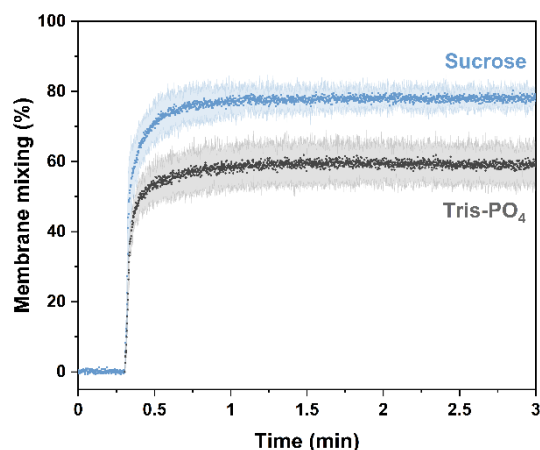


**Fig. S30.** Charge-mediated membrane mixing of hybrid LUVs with 10 mol% of charged lipids in 200 mM sucrose (blue trace) and 20 mM Tris (pH 8.0), 20 mM  $H_3PO_4$  (gray trace). LUVs were composed of 89–90 mol% PDMS-*g*-PEO and 10 mol% DOTAP or soy PS. Membranes of LUVs containing soy PS were tagged with 0.5 mol% PE-Rho and 0.5 mol% PE-NBD. Tagged and non-tagged LUVs were mixed in molar ratio 1:1; final concentration of LUVs was 100  $\mu$ M. 100 % was obtained by solubilizing vesicles with Triton X-100. Error bars represent SD from  $n = 3$ .

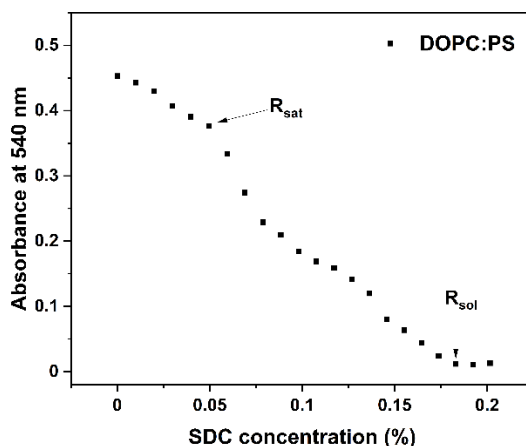


**Fig. S31.** Solubilization of DOPC:PS (70:30, molar ratio) LUVs by sodium deoxycholate cholate (SDC). Arrows indicate saturation ( $R_{sat}$ ) and solubilization point ( $R_{sol}$ ).

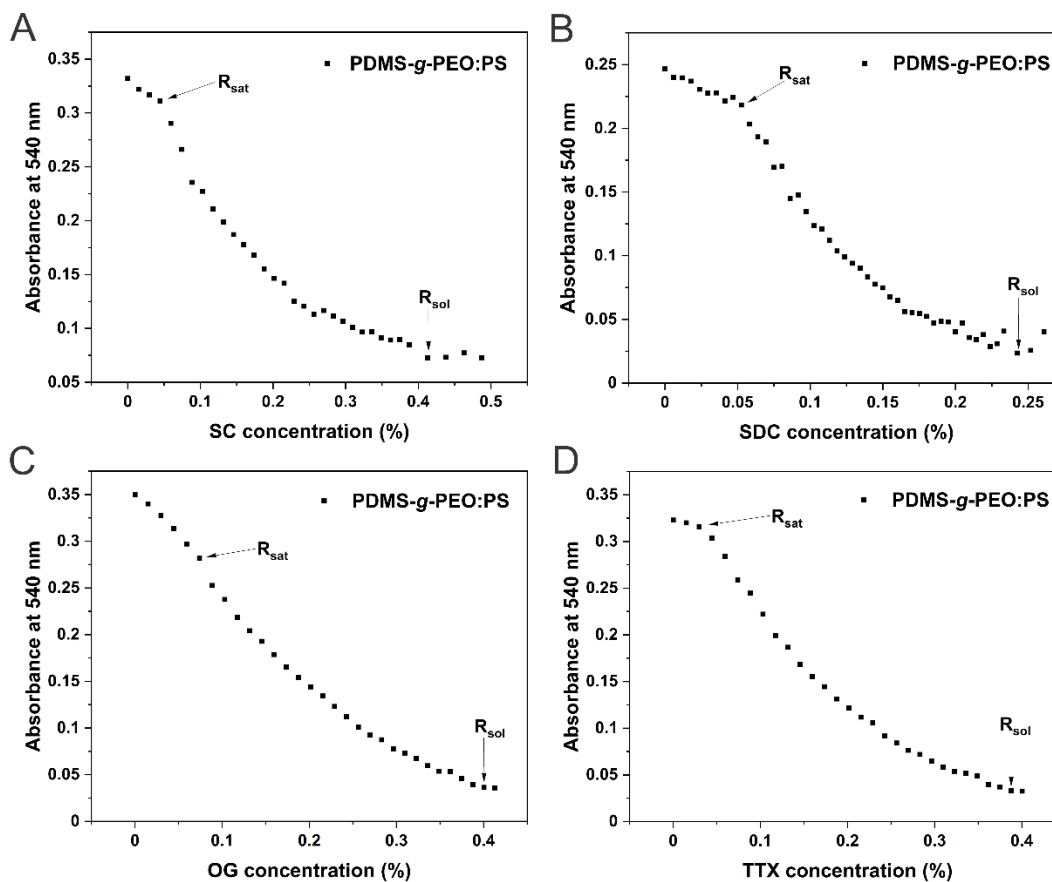


**Fig. S32.** Solubilization of PDMS-g-PEO:PS (70:30, molar ratio) LUVs by sodium cholate (SC) (A), sodium deoxycholate (SDC) (B), octyl glucoside (OG) (C) and Triton X-100 (TTX) (D).

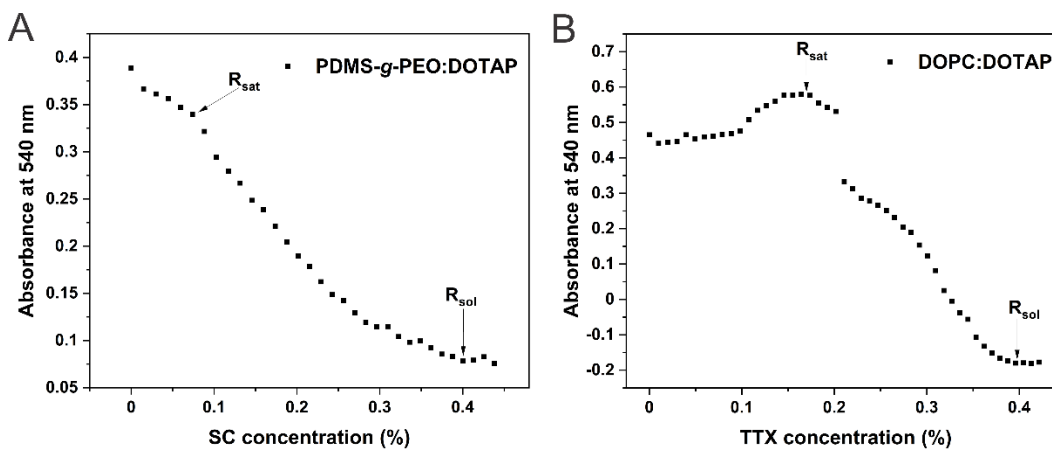


**Fig. S33.** Solubilization of PDMS-g-PEO:DOTAP (70:30, molar ratio) LUVs by sodium cholate (SC) (A) and Triton X-100 (TTX) (B).

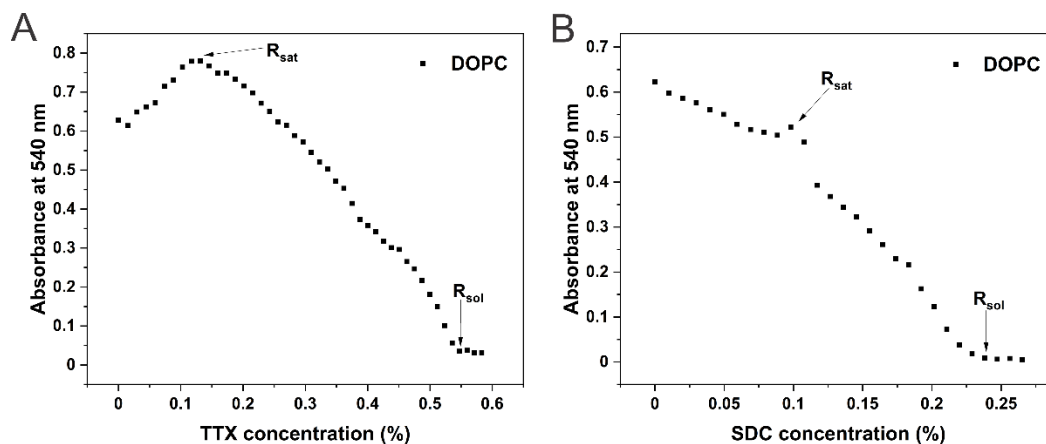


**Fig. S34.** Solubilization of DOPC (70:30, molar ratio) LUVs by Triton X-100 (TTX) (A) and sodium deoxycholate (SDC) (B).

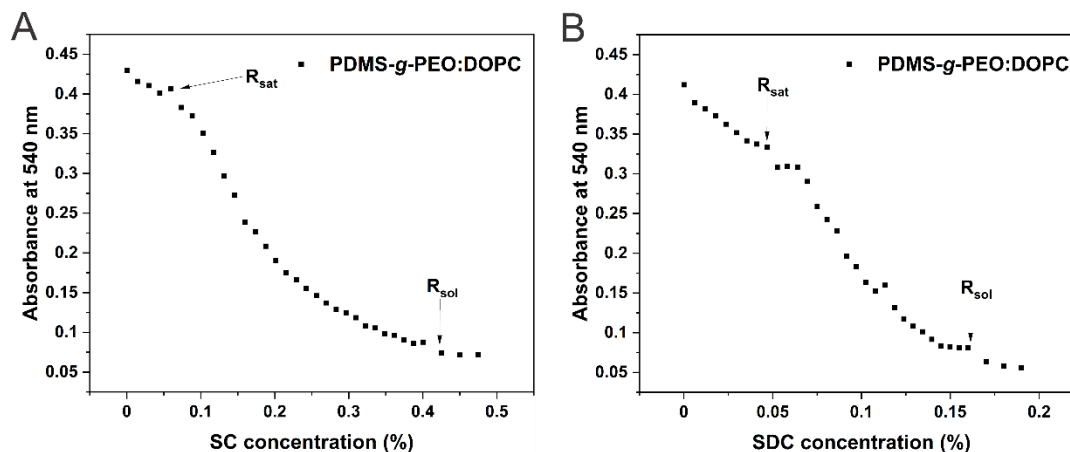


**Fig. S35.** Solubilization of PDMS-g-PEO:DOPC (70:30, molar ratio) LUVs by sodium cholate (SC) (A) and sodium deoxycholate (SDC) (B).

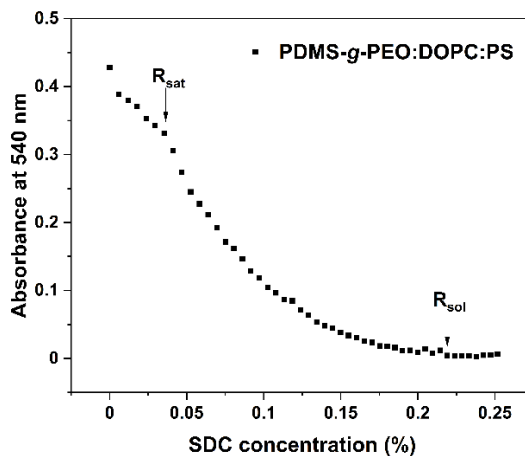


**Fig. S36.** Solubilization of PDMS-g-PEO:DOPC:soy PS (70:20:10, molar ratio) LUVs by sodium deoxycholate (SDC).

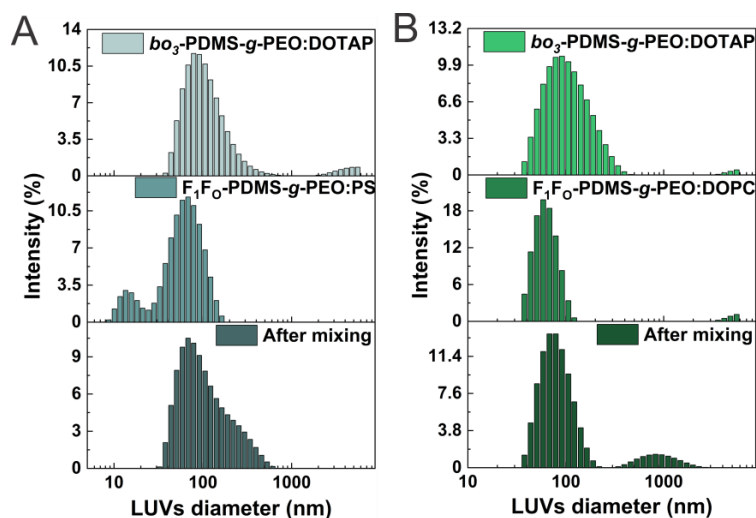


**Fig. S37.** Hybrids size distribution by intensity, determined by DLS.  $bo_3$  oxidase was reconstituted with SC  $R_{sat}$ , and  $F_1F_0$ -ATPase with SDC  $R_{sol}$ . The vesicles correspond to lower activity in Figure 7D. (A)  $bo_3$  oxidase was reconstituted into PDMS-*g*-PEO:DOTAP (70:30, molar ratio) LUVs, and  $F_1F_0$ -ATPase into PDMS-*g*-PEO:PS (70:30, molar ratio) LUVs. (B)  $bo_3$  oxidase was reconstituted into PDMS-*g*-PEO:DOTAP (70:30, molar ratio) LUVs, and  $F_1F_0$ -ATPase into PDMS-*g*-PEO:DOPC (70:30, molar ratio) LUVs.

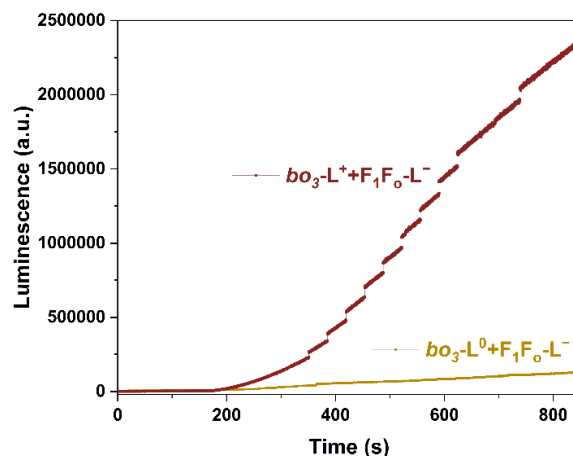


**Fig. S38.** Respiratory-driven ATP synthesis after charge-mediated fusion of neutral or positively charged lipid LUVs with reconstituted  $bo_3$  oxidase and negatively charged lipid LUVs with reconstituted  $F_1F_0$ -ATPase. Charged liposomes were composed of DOPC:DOTAP or DOPC:PS (70:30, molar ratio). Change in luminescence over time corresponding to synthesized ATP. ATP can be synthesized by  $F_1F_0$ -ATPase only if both proteins are in the same vesicle,  $\Delta pH$  is established by  $bo_3$  oxidase and vesicles are proton tight.

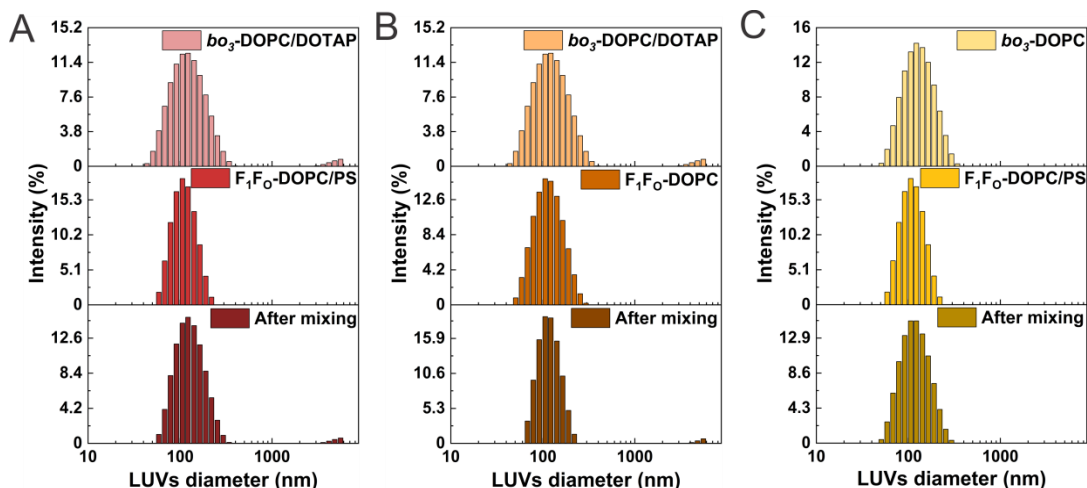


**Fig. S39.** Liposomes size distribution by intensity, determined by DLS. Upon reconstitution of MPs,  $bo_3$ -lipid-LUVs and  $F_1F_0$ -lipid-LUVs were incubated together, at room temperature, for 10 min (at 500 rpm). (A)  $bo_3$  oxidase was reconstituted into DOPC:DOTAP (70:30, molar ratio) LUVs, and  $F_1F_0$ -ATPase into DOPC:PS (70:30, molar ratio) LUVs. (B)  $bo_3$  oxidase was reconstituted into DOPC:DOTAP (70:30, molar ratio) LUVs, and  $F_1F_0$ -ATPase into DOPC LUVs. (C)  $bo_3$  oxidase was reconstituted into DOPC LUVs, and  $F_1F_0$ -ATPase into DOPC:PS (70:30, molar ratio) LUVs.

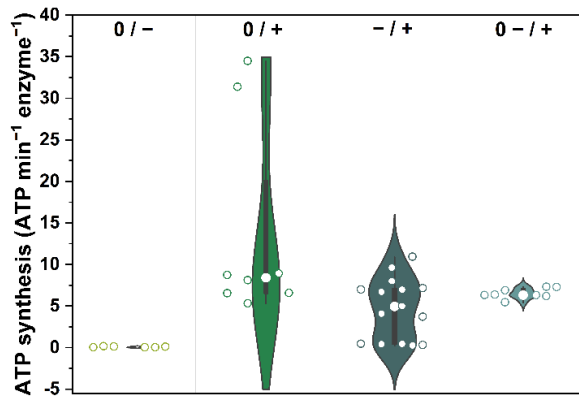


**Fig. S40.** Respiratory-driven ATP synthesis in hybrid LUVs. Hybrids were composed of PDMS-*g*-PEO:DOTAP (+), PDMS-*g*-PEO:PS (-) or PDMS-*g*-PEO:DOPC (0) (all at 70:30, molar ratio).  $bo_3$  oxidase was reconstituted into cationic or neutral LUVs, and ATPase into anionic or neutral LUVs. 0-/+ indicates reconstitution of ATPase in hybrids containing 20 mol% DOPC and 10 mol% soy PS, and subsequent fusion with cationic  $bo_3$ -LUVs.

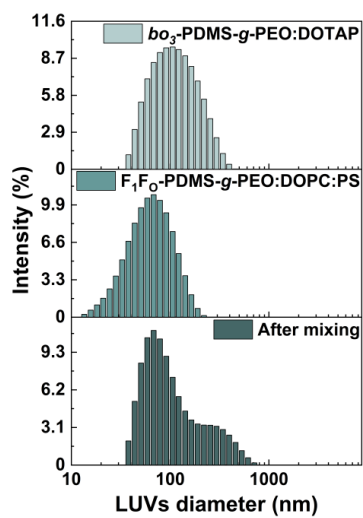


**Fig. S41.** Proteo-hybrid-LUVs size distribution by intensity, determined by DLS (before and after fusion). *bo*<sub>3</sub> oxidase was reconstituted into cationic hybrids containing 30 mol% DOTAP and F<sub>1</sub>F<sub>0</sub>-ATPase into anionic hybrids containing 10 mol% soy PS.

### Delivery of $bo_3$ oxidase-ATTO 425 into hybrid GUVs

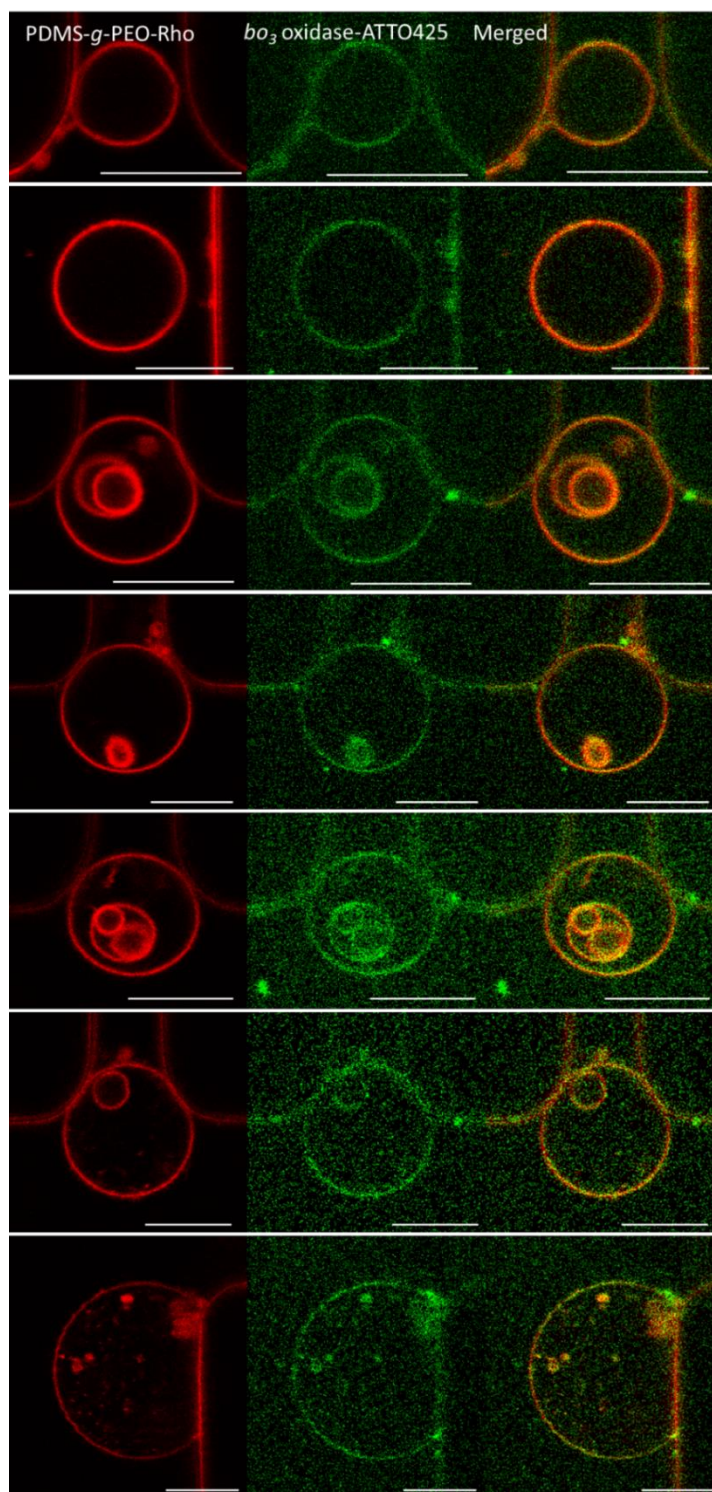


**Fig. S42.** Delivery of  $bo_3$  oxidase from cationic hybrid LUVs into anionic hybrid GUVs trapped in microfluidic device.  $bo_3$  oxidase-ATTO 425 (green) was delivered into anionic GUVs upon GUV-LUV fusion.  $bo_3$  oxidase was reconstituted into cationic hybrid (PDMS-g-PEO:DOTAP = 70:30, mol%) LUVs. Scale bar: 10  $\mu$ m.

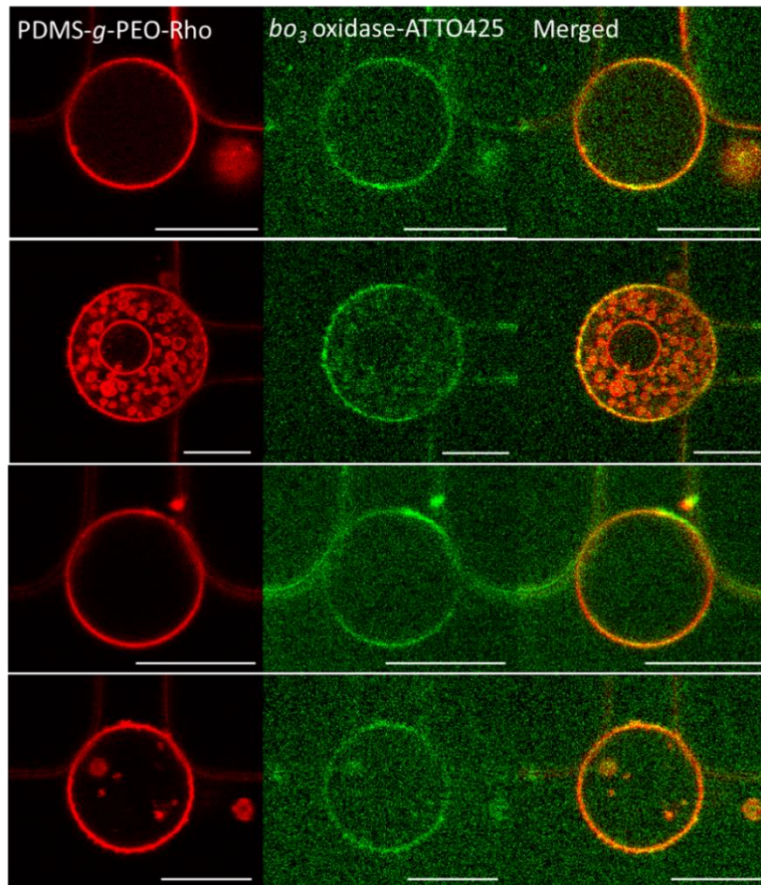


**Fig. S43.** Delivery of  $bo_3$  oxidase from cationic lipid LUVs into anionic hybrid GUVs trapped in microfluidic device.  $bo_3$  oxidase-ATTO 425 (green) was delivered into anionic GUVs upon GUV-LUV fusion.  $bo_3$  oxidase was reconstituted into cationic lipid (DOPC:DOTAP = 70:30, mol%) LUVs. Scale bar: 10  $\mu$ m.

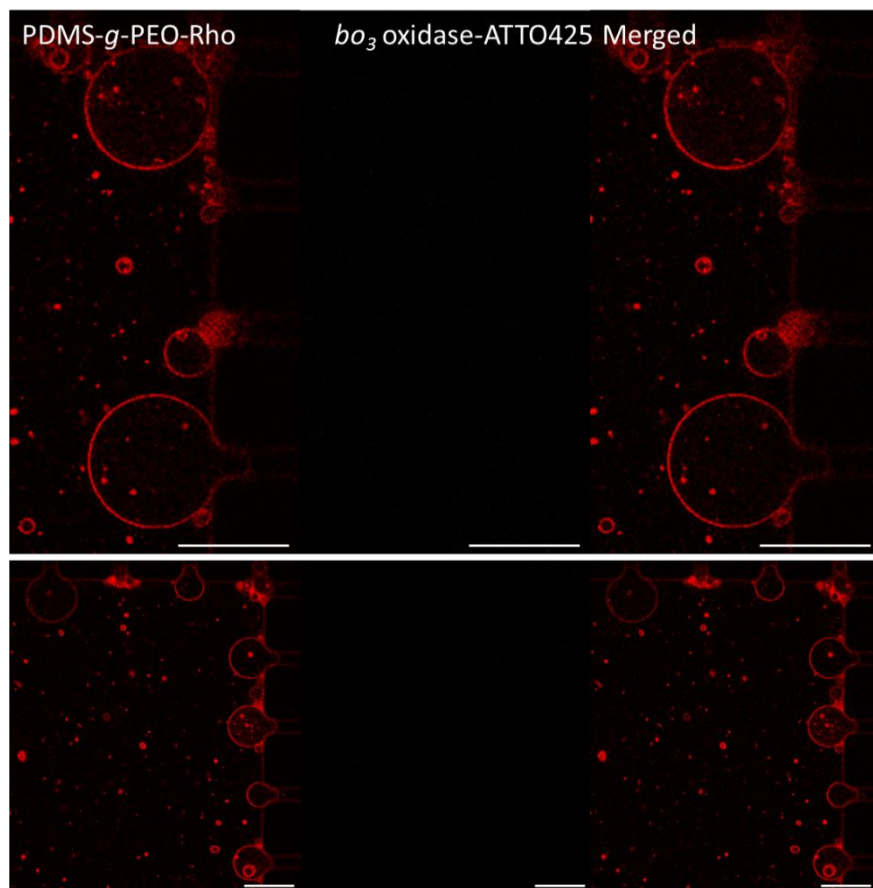


**Fig. S44.** Anionic hybrid GUVs trapped in microfluidic device before flushing with *bo*<sub>3</sub>-ATTO425-hybrid-LUVs. Hybrid GUVs were tagged with PDMS-*g*-PEO-Rho. Scale bar: 30  $\mu$ m.

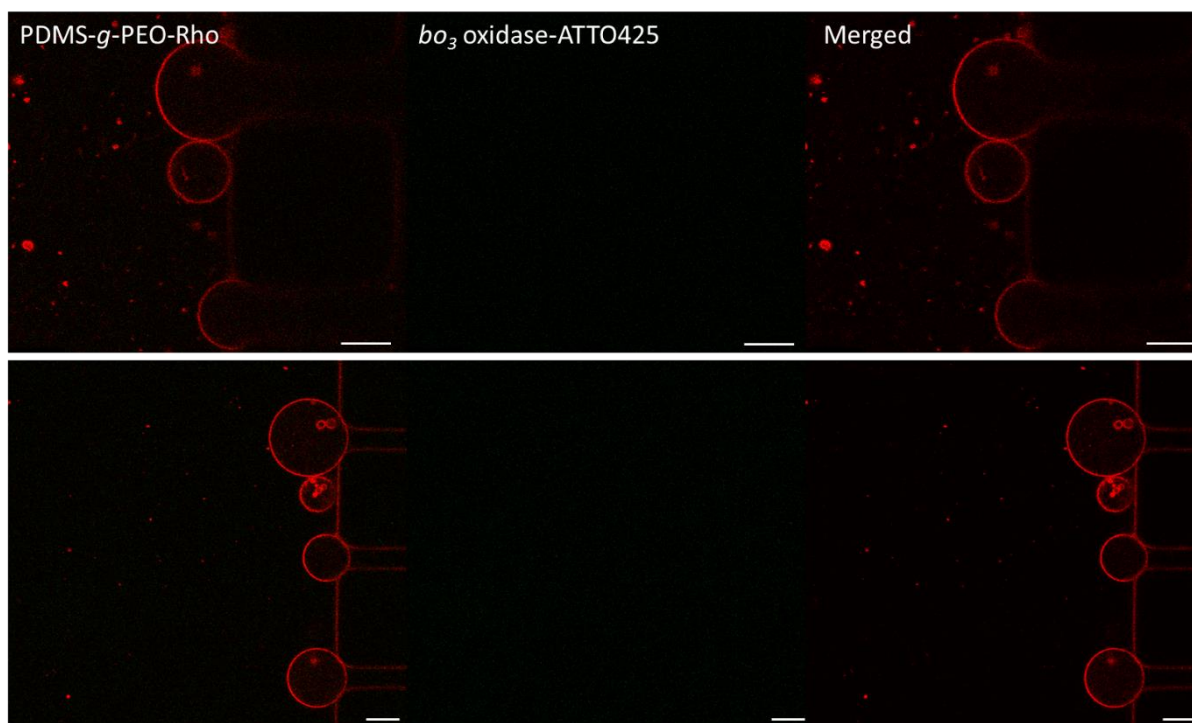


**Fig. S45.** Anionic hybrid GUVs trapped in microfluidic device before flushing with  $bo_3$ -ATTO425-lipid-LUVs. Hybrid GUVs were tagged with PDMS-*g*-PEO-Rho. Scale bar: 10  $\mu$ m.

## SI References:

1. M. Chemin, P.-M. Brun, S. Lecommandoux, O. Sandre, J.-F. Le Meins, Hybrid polymer/lipid vesicles: fine control of the lipid and polymer distribution in the binary membrane. *Soft Matter* 8(10):2867 (2012).
2. H. L. Frericks, D. H. Zhou, L. L. Yap, R. B. Gennis, C. M. Rienstra, Magic-angle spinning solid-state NMR of a 144 kDa membrane protein complex: E. coli cytochrome bo3 oxidase. *J. Biomol. NMR* 36(1):55-71 (2006).
3. R. R. Ishmukhametov, M.A. Galkin, S. B. Vik, Ultrafast purification and reconstitution of His-tagged cysteine-less Escherichia coli F1Fo ATP synthase. *Biochim. Biophys. Acta Bioenerg.* 1706(1):110-116 (2005).
4. L. Otrin, N. Marušič, C. Bednarz, T. Vidaković-Koch, I. Lieberwirth, K. Landfester, K. Sundmacher, Toward Artificial Mitochondrion: Mimicking Oxidative Phosphorylation in Polymer and Hybrid Membranes. *Nano Lett.* 17(11):6816-6821 (2017).
5. N. Marušič, L. Otrin, Z. Zhao, R. B. Lira, F. L. Kyrilis, F. Hamdi, P. L. Kastiris, T. Vidaković-Koch, I. Ivanov, K. Sundmacher, R. Dimova, Constructing artificial respiratory chain in polymer compartments: Insights into the interplay between bo3 oxidase and the membrane. *Proc. Natl. Acad. Sci. U.S.A.* 117(26):15006–15017 (2020).